

Wingbeat Shape Modulation for Flapping-Wing Micro-Air-Vehicle Control During Hover

David B. Doman,* Michael W. Oppenheimer,† and David O. Sighorsson‡
U.S. Air Force Research Laboratory, Wright-Patterson Air Force Base, Ohio 45433-7531

DOI: 10.2514/1.47146

A new method of controlling a flapping-wing micro air vehicle by varying the velocity profiles of the wing strokes is presented in this manuscript. An exhaustive theoretical analysis along with simulation results show that this new method, called split-cycle constant-period frequency modulation, is capable of providing independent control over vertical and horizontal body forces as well as rolling and yawing moments using only two physical actuators, whose oscillatory motion is defined by four parameters. An actuated bob-weight is introduced to enable independent control of pitching moment. A general method for deriving sensitivities of cycle-averaged forces and moments to changes in wingbeat kinematic parameters is provided, followed by an analytical treatment for a case where the angle of attack of each wing is passively regulated and the motion of the wing spar in the stroke plane is driven by a split-cycle waveform. These sensitivities are used in the formulation of a cycle-averaged control law that successfully stabilizes and controls two different simulation models of the aircraft. One simulation model is driven by instantaneous aerodynamic forces derived from blade-element theory, while the other is driven by an empirical representation of an unsteady aerodynamic model that was derived from experiments.

I. Introduction

WEIGHT and volume constraints on flapping-wing micro air vehicles (MAVs) drive the desire to use as few actuators as possible while achieving a high level of controlled maneuverability using the simplest possible controller. The best way of achieving this objective is an open question and represents a multidisciplinary design problem wherein vehicle controllability must be considered from the outset. Additionally, the issue of determining an adequate level of fidelity for model-based control design for flapping-wing aircraft, which are influenced by unsteady aerodynamic phenomena, has not been settled. This exposition addresses each of these open problems.

To address the problem of reducing the number of required actuators for highly maneuverable flight, a new control strategy, called split-cycle constant-period frequency modulation, is presented, which shapes each wingbeat velocity profile and enables independent control of vertical and horizontal body forces and rolling and yawing moments using only two physical actuators. Thus, four degrees of freedom can be controlled using two physical actuators whose oscillatory behavior is parameterized by four inputs. The overall objective of achieving a high level of maneuverability using a reduced set of actuators is thereby achieved, which represents an advance over the state of the art where the number of physical actuators was required to be greater than or equal to the number of independent degrees of freedom to be controlled [1–7].

An aircraft concept is presented that is equipped with three bimorph piezoelectric actuators. Two of these actuators manipulate

the wings to follow split-cycle wing position profiles, while the third manipulates a bob-weight that allows the vehicle center of mass to shift for the purpose of enabling pitch control. The result is the ability to independently control five degrees of freedom using three physical actuators. Unlike some flapping-wing MAV designs [5,6], this aircraft is designed to be capable of hovering and maneuvering using only two wings and a bob-weight, without the need for conventional empennage control effectors.

A general framework is presented for computing a control-oriented model for flapping-wing MAVs. This framework is used to address the issue of determining an adequate level of modeling fidelity for a model-based control law that must stabilize and control the proposed vehicle. The method begins by constructing a cycle-averaged model of the aerodynamic forces and moments that is similar to those found in the literature [2,3,8,9]. However, in the present method, the sensitivities of these cycle-averaged forces and moments with respect to the wingbeat kinematic parameters that can be manipulated are computed in order to form a matrix of cycle-averaged control derivatives that can be used for control synthesis. The method is general in the sense that the aerodynamic control derivatives can be extracted from high-fidelity numerical aerodynamic models, experimental measurements, or simple blade-element models depending upon the desired level of controller performance. In the interest of determining the level of adequate fidelity for a model-based controller, an analytical blade-element aerodynamic model is presented for the proposed aircraft. The control derivatives are then analytically derived and used to design a controller. These sensitivities are used in the formulation of a cycle-averaged control law that successfully stabilizes and controls two different simulation models of the aircraft. One simulation model is driven by instantaneous aerodynamic forces derived from blade-element theory, while the other is driven by an empirical representation of an unsteady aerodynamic model that was derived from experiments. Simulation results indicate that a cycle-averaged blade-element-model-based controller is robust to the aerodynamic modeling error introduced by the control-oriented modeling assumptions. Additionally, it is noted that stability and tracking performance for flapping-wing aircraft must be interpreted in terms of how the aircraft is targeted to equilibrium points that it will ultimately orbit. Limit cycles about target set points are unavoidable [10–12] because flapping wings, by their very nature, produce periodic forces and moments.

Finally, by computing an analytical control-oriented model from blade-element theory, a direct link between the aircraft design and the

Presented as Paper 6160 at the AIAA Guidance, Navigation, and Control Conference, Chicago, IL, 10–13 August 2009; received 11 September 2009; revision received 10 December 2009; accepted for publication 22 December 2009. This material is declared a work of the U.S. Government and is not subject to copyright protection in the United States. Copies of this paper may be made for personal or internal use, on condition that the copier pay the \$10.00 per-copy fee to the Copyright Clearance Center, Inc., 222 Rosewood Drive, Danvers, MA 01923; include the code 0731-5090/10 and \$10.00 in correspondence with the CCC.

*Senior Aerospace Engineer, Control Design and Analysis Branch, 2210 Eighth Street, Suite 21; David.Doman@wpafb.af.mil. Associate Fellow AIAA.

†Senior Electronics Engineer, Control Design and Analysis Branch, 2210 Eighth Street, Suite 21; Michael.Oppenheimer@wpafb.af.mil. Senior Member AIAA.

‡National Research Council Associate, Control Design and Analysis Branch, 2210 Eighth Street, Suite 21; David.Sighorsson@afmcx.net. Member AIAA.

vehicle's controllability can be established. This feature allows designers to consider controllability early in the design process and enables insights into control strategies that might be obfuscated by purely numerical representations of the aerodynamics. Insights into vehicle physics and design are highlighted throughout the analytical development.

II. Vehicle Concept

The first takeoff of an insect-scale flapping-wing MAV was achieved by an aircraft called RoboFly that was developed at Harvard University by Wood [13]. A key feature that led to its successful first flight is that the vehicle was minimally actuated. RoboFly uses a single bimorph piezoelectric actuator to impart symmetric motion to two wings. The wing angle of inclination with respect to the stroke plane is regulated by passive wing rotation joints resulting in planform motion that is similar to that of a dipteran insect. This passive rotation of the planform about the spar eliminates the need for added weight and complexity associated with actuators that actively rotate the planform about the spar. The first flight at Harvard resulted in unregulated flight up a pair of wires that constrained the vehicle motion to vertical translation. In the present paper, a vehicle concept similar to the Harvard Robofly is proposed, along with a control strategy, that would enable controlled six-degree-of-freedom (DOF) flight of the fuselage without the need for artificial motion constraints.

A. Design Features

A diagram of the proposed vehicle is shown in Fig. 1. The main differences between the proposed vehicle and the RoboFly are that the new control-configured aircraft would be equipped with independently actuated wings and an actuated bob-weight that allows the vehicle center of gravity to be manipulated for control purposes. The wings rotate about hinges at the wing root. A linkage-based transmission translates the tangential motion of the tip of a bimorph piezoelectric actuator into rotational motion of the wings in the stroke plane. The linkage elements are designed to achieve impedance matching between the wing and actuator forces as well as amplify the relatively small motion of the tip of the bimorph strip into large angular displacements of the wing root. The planforms are connected to the movable wing roots by a limited hinge or flexure joint that provides for passive rotation of the wing. This hinge allows

the wing to passively flip over as the wing reverses direction at the end of each stroke and enables the chord to rotate about the axis of the spar in a manner that approximates the wing-twisting motion that has been observed in dipteran insects [14]. As the wing rotates through the stroke plane, dynamic pressure acting on the wing tends to cause it to feather into the wind; however, as shown in Fig. 2, a flexure hinge joint is designed such that the spar and root structure interfere at an angle set by the designer that prevents the wing from overrotating. This interference causes the wing to hold a constant angle of attack relative to the stroke plane once a critical dynamic pressure is reached. The bimorph piezoelectric actuators and the carbon fiber substrate to which they are mounted are cantilevered to the fuselage. In the case of the wings, the actuator assembly and linkage, together with the wing, form a spring-mass-damper system that has a known resonant frequency. The actuator assembly for the bob-weight is simply used to control the mean pitch attitude of the fuselage. In the single actuator Harvard experiments, the dynamic system was driven at resonance [15] for maximum energy efficiency to achieve flight. In the present problem, each wing-linkage-actuator system is nominally driven at a hover frequency that is defined as the frequency at which the cycle-averaged lift is equal to the aircraft weight. The term *hover* is to be interpreted in a time-averaged sense because, as we will show, the aircraft is in constant motion due to the periodic nature of the forces and moments produced by the flapping wings. The closest approximation of hover that can be achieved is that of a high-frequency, low-amplitude limit cycle about a mean position [12].

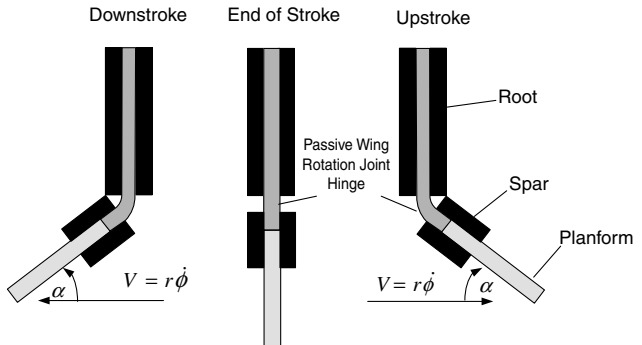


Fig. 2 Detail of wing hinge flexure joint.

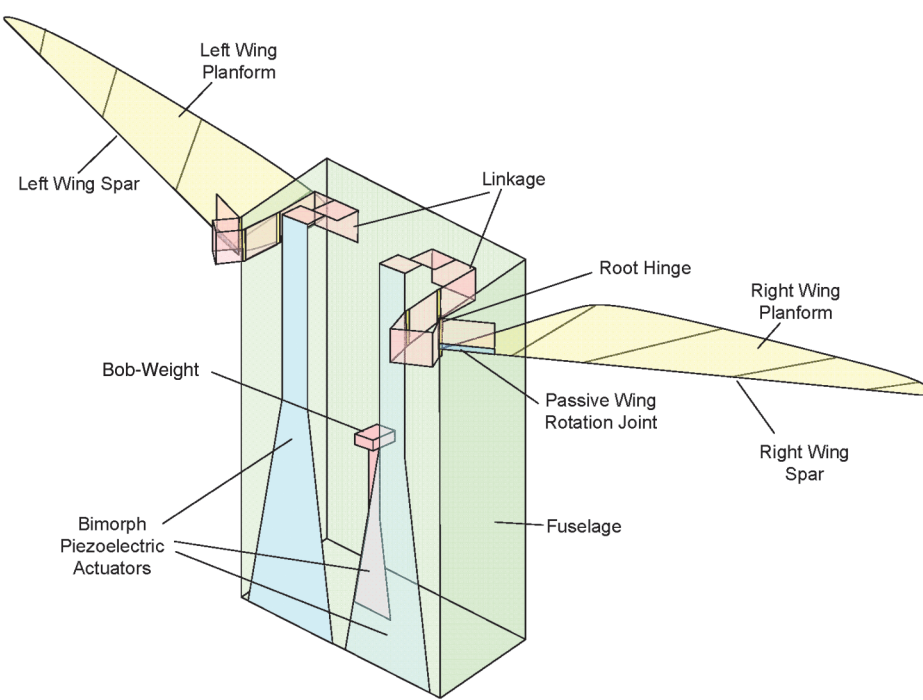


Fig. 1 General assembly of a control-configured MAV equipped with independently actuated wings and an actuated bob-weight.

B. Control Strategy

The coordinate frames and wing angles used in the development of the control strategy are illustrated in Fig. 3. The vehicle is designed to mimic dipteran insect flight; thus, the angular velocity of each wing in its respective stroke plane $\dot{\phi}$ must be a time-varying function that is equal to zero at the extreme limits of wing position. It is assumed that the wing position, in the stroke plane, can be controlled directly via a high bandwidth piezoelectric bimorph actuator. To begin the development, a simple cosine function is selected to drive the stroke plane rotation angle of each wing:

$$\phi = \cos \omega t \quad (1)$$

The maximum value of this angle occurs when either wing reaches its maximum displacement towards the ventral side of the vehicle. Assuming that the frequency of the oscillating wing is held constant over the segment of interest for each wingbeat cycle, the angular velocity of the wing is given by

$$\dot{\phi} = -\omega \sin \omega t \quad (2)$$

Note that the units of ϕ are in radians and that the amplitude of the wing rotation in the stroke plane is taken to be ± 1 rad, which closely approximates the rotation limits used in the Harvard RoboFly and those observed in some flying insects such as the hawkmoth *Manduca sexta* [16]. The frequency of the oscillator that drives the actuator is selected as one of the control input variables that is used to enable multidegree-of-freedom flight; however, this frequency is allowed to change at key points in the wingbeat cycle, namely at the ends of the stroke when $\phi = 1$, $\dot{\phi} = 0$ and $\phi = -1$, $\dot{\phi} = 0$. If the wingbeat frequency is held constant over each cycle and the angles of attack for each stroke are equivalent, then the cycle-averaged longitudinal force along the x body axis is always finite and positive, while the cycle-averaged z body force is always zero. Such conditions make it possible to achieve a practical condition that approximates hover and allows altitude tracking [12]; however, to enable a

vehicle to achieve multidegree-of-freedom flight, an additional control input variable must be introduced.

To achieve a nonzero cycle-averaged body force in the z direction, using wings equipped with passive wing rotation joints as described above, the stroke plane angular velocity of each wing must be temporally asymmetric over the wingbeat cycle; i.e., the wing velocity profiles of the upstroke and downstrokes must be different. Ennos [17] presents biological evidence for differing upstroke and downstroke velocities. One way to induce temporal asymmetry across each wingbeat is to parameterize the waveforms that define the motion of each wing in the stroke plane in terms of temporally symmetric and asymmetric components. The new technique that is proposed to produce this desired behavior is referred to as split-cycle constant-period frequency modulation. The fundamental idea is to piece together two cosine waves of different frequencies over one complete wingbeat cycle, i.e., an upstroke and a downstroke. The period of the cycle is fixed by the symmetric or fundamental frequency, while the speed of each stroke within the cycle is governed by an asymmetric frequency or split-cycle parameter.

A detailed discussion of the mathematical construction of these split-cycle waveforms is provided by Doman et al. [18] and Oppenheimer et al. [19]. In short, the split-cycle control strategy generates time-varying upstroke and downstroke wing position commands that are defined by

$$\phi_U(t) = \cos[(\omega - \delta)t], \quad 0 \leq t < \frac{\pi}{(\omega - \delta)} \quad (3)$$

$$\phi_D(t) = \cos[(\omega + \sigma)t + \xi], \quad \frac{\pi}{(\omega - \delta)} \leq t < \frac{2\pi}{\omega} \quad (4)$$

where

$$\sigma = \frac{\delta\omega}{\omega - 2\delta} \quad (5)$$

and

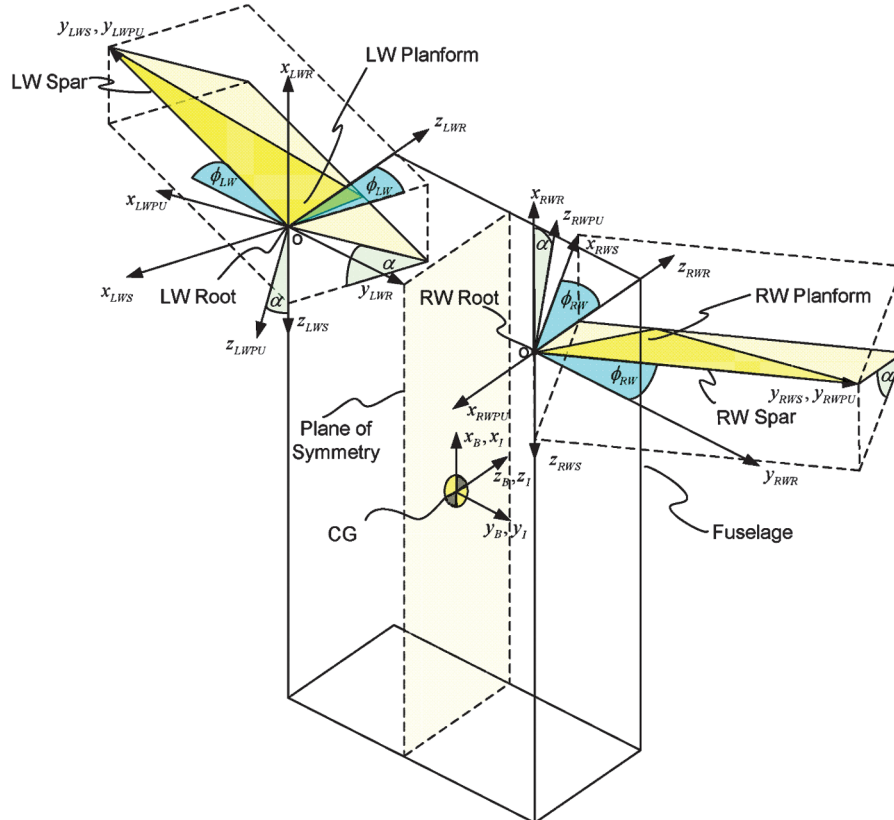


Fig. 3 Relationship between body, root, spar, left-, and right-wing-planform axis systems on upstroke.

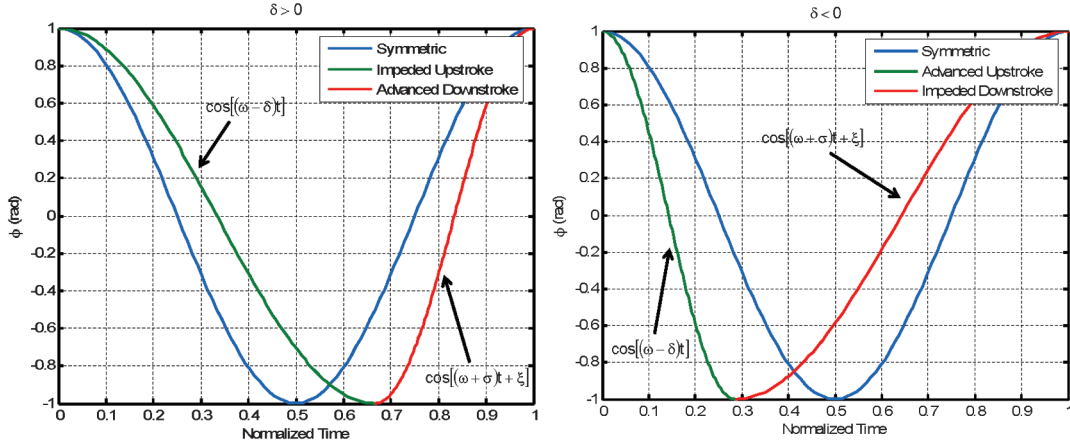


Fig. 4 Split-cycle waveforms.

$$\xi = \frac{-2\pi\delta}{\omega - 2\delta} \quad (6)$$

Thus, the waveform that drives the angular position of each wing in the stroke plane is completely defined by the symmetric frequency ω and the asymmetric frequency or split-cycle parameter δ , where $\delta < \frac{\omega}{2}$. The stroke plane angular velocity of each wing over each split-cycle interval is given by

$$\dot{\phi}_U(t) = -(\omega - \delta) \sin[(\omega - \delta)t], \quad 0 \leq t < \frac{\pi}{(\omega - \delta)} \quad (7)$$

$$\dot{\phi}_D(t) = -(\omega + \sigma) \sin[(\omega + \sigma)t + \xi], \quad \frac{\pi}{(\omega - \delta)} \leq t < \frac{2\pi}{\omega} \quad (8)$$

Figure 4 shows the wingbeat position profile for $\delta > 0$ and $\delta < 0$ along with a symmetric wingbeat. The split-cycle parameter δ for each wing, along with ω for each wing, become control parameters. Hence, the waveforms that drive the left and right wing positions are defined by the following control parameters: ω_{LW} , δ_{LW} , ω_{RW} , and δ_{RW} , respectively.

The control strategies proposed in this manuscript are based on the assumption that the bandwidth of the closed-loop fuselage control system is much less than the flapping frequency required to achieve a quasi-hover condition. If nonoscillatory control forces and inertial measurements were available for feedback, one could use conventional control design techniques to synthesize feedback control laws that produce favorable closed-loop responses. However, because of the nature of the aerodynamic forces produced by flapping wings, time-varying high-frequency oscillatory forces and moments must be manipulated to impart desired motion to the fuselage. Under this constraint, the tracking behavior of the fuselage will, under the best of conditions, be characterized by low-amplitude and high-frequency limit cycles about desired set points. Towards this end, the relationships between the cycle-averaged forces and moments and the control input parameters that define the characteristics of the oscillators that drive the wing positions are computed. Feedback control laws based on cycle-averaged forces and moments will be designed to allow a vehicle to track desired angular and spatial positions in a mean sense.

The general method used to compute the cycle-averaged aerodynamic forces and their sensitivities to variations in the parameters that define the wingbeat kinematics will now be presented. The method is general in the sense that the aerodynamic control derivatives can be extracted from high-fidelity numerical aerodynamic models, experimental measurements, or simple blade-element models depending upon the desired level of controller performance. $G(t)$ is defined to be a generalized force that is aligned with a principal body-axis direction. Thus, $G(t)$ may represent either a force or a moment. To compute the cycle-averaged generalized force associated with each wing, an integral of the following form is evaluated:

$$\bar{G} = \frac{\omega}{2\pi} \int_0^{\frac{2\pi}{\omega}} G(\phi(t)) dt \quad (9)$$

Since the introduction of the split-cycle parameter changes the frequency of the cosine wave when $(\omega - \delta)t = \pi$ in each cycle, it is convenient to split the integral as follows:

$$\bar{G} = \frac{\omega}{2\pi} \left[\int_0^{\frac{\pi}{\omega-\delta}} G(\phi_U(t)) dt + \int_{\frac{\pi}{\omega-\delta}}^{\frac{2\pi}{\omega}} G(\phi_D(t)) dt \right] \quad (10)$$

The control derivatives associated with a generalized cycle-averaged force are calculated by computing the partial derivative with respect to each control input variable about the hover frequency ω_o . The control derivatives at hover are

$$\bar{G}_{\Delta\omega_{LW}} = \frac{\partial \bar{G}}{\partial \omega_{LW}} \Big|_{\omega_{LW}=\omega_o, \delta_{LW}=0} \quad (11)$$

$$\bar{G}_{\delta_{LW}} = \frac{\partial \bar{G}}{\partial \delta_{LW}} \Big|_{\omega_{LW}=\omega_o, \delta_{LW}=0} \quad (12)$$

$$\bar{G}_{\Delta\omega_{RW}} = \frac{\partial \bar{G}}{\partial \omega_{RW}} \Big|_{\omega_{RW}=\omega_o, \delta_{RW}=0} \quad (13)$$

$$\bar{G}_{\delta_{RW}} = \frac{\partial \bar{G}}{\partial \delta_{RW}} \Big|_{\omega_{RW}=\omega_o, \delta_{RW}=0} \quad (14)$$

where the hover frequency [12] is given by

$$\omega_o = \sqrt{\frac{2 \text{ mg}}{\rho I_A C_L(\alpha)}} \quad (15)$$

These control derivatives can be used to design the control allocation portion of a six-DOF control law for the proposed flapping-wing MAV. The above calculations could be carried out numerically if high-fidelity unsteady computational fluid dynamic simulations or experimental measurements were available and it was determined that lower-fidelity methods produced model-based controllers that were incapable of providing adequate performance. As will be shown throughout the remainder of the exposition, a blade-element-based aerodynamic model is sufficiently accurate to produce controllers that provide adequate performance when applied to a simulation model that is driven by unsteady aerodynamics. The blade-element model has the added advantage that cycle-averaging calculations can be carried out analytically and the resulting model shows a clear and direct tie between key vehicle design parameters and its controllability.

III. Instantaneous Blade-Element Model

Strictly speaking, all mathematical models of physical systems are idealized representations of systems that cannot physically exist. The critical issue for the control engineer is to formulate a model of a physical system of interest that is of suitable fidelity, which enables a control system to be designed that is robust to errors resulting from the modeling process. A control-oriented model should be computationally efficient so that dynamic simulations of the closed-loop physical system run in a reasonable period of time; furthermore, it is desirable for such models to provide a direct link between vehicle controllability and the aircraft design parameters.

The purpose of this development is to derive an idealized analytical model that will allow one to study the dynamic behavior of the aircraft under consideration and to formulate and ultimately test the proposed control strategies using nonreal-time simulations that relax many of the key assumptions used to derive the analytical model. The following assumptions are made in the formulation of this analytical control-oriented model: no aerodynamic interactions exist between the left and right wings, nor between the wings and the fuselage; two-dimensional sectional aerodynamic coefficients are known and constant throughout each stroke; passive wing rotation joints are on a limit when the corresponding wing's stroke plane angular velocity is nonzero; aerodynamic forces and moments are the sole result of wing motion, i.e., only flight conditions in the neighborhood of hover are considered; and piezoelectric actuator bandwidth is much greater than the wingbeat frequency required to hover.

The dynamic analysis of the vehicle requires the use of several coordinate frames. This is because the signs of aerodynamic forces and moments differ from the left wing to the right wing. Furthermore, the signs of the forces and moments are dependent upon the direction of the wing stroke, i.e., upstroke or downstroke. The aerodynamic forces and moments can be conveniently written in certain intermediate frames; however, it will be necessary to transform them into a body-fixed and ultimately an inertial coordinate frame in order to write the equations of motion of the fuselage. The coordinate frame and angle definitions are illustrated in Fig. 3. A comprehensive table containing the definitions of the numerous coordinate frames and rotation matrices is provided by Doman et al. [18].

A. Instantaneous Aerodynamic Forces and Centers of Pressure in Wing Planform Frames

The aerodynamic forces are derived, using blade-element theory, for wings that have two degrees of freedom, namely, angular displacement $\phi(t)$ about the wing root in the stroke plane and angular displacement of the planform about a passive rotation hinge joint, which is equivalent to wing angle of attack α , in still air. The planform is taken to be a rigid flat plate and the lift and drag, produced by each wing [18], can be expressed as

$$L = k_L \dot{\phi}(t)^2 \quad D = k_D \dot{\phi}(t)^2 \quad (16)$$

where

$$k_L \triangleq \frac{\rho}{2} C_L(\alpha) I_A \quad k_D \triangleq \frac{\rho}{2} C_D(\alpha) I_A \quad (17)$$

and I_A is the area moment of inertia of the planform about the axis of the root-hinge, ρ is the atmospheric density, and $C_D(\alpha)$ and $C_L(\alpha)$ are the lift and drag coefficients. Empirical expressions for lift and drag coefficients [20], which were obtained from low-Reynolds-number experiments, are used in this work:

$$C_D(\alpha) = 1.92 - 1.55 \cos(2.04\alpha - 9.82) \\ C_L(\alpha) = 0.225 + 1.58 \sin(2.13\alpha - 7.2) \quad (18)$$

where α is in degrees.

B. Expression of Aerodynamic Forces and Centers of Pressure in the Body Frame

Using the relationships between the body, roots, spars, upstroke-planform, and downstroke-planform axis systems defined in Doman et al. [18], the instantaneous values of lift and drag on each wing can be transformed into the body-axis coordinate frame. If the air mass is quiescent, then the relative wind is parallel to the stroke plane, which is coincident with the x - y planes of the local spar frames. Therefore, the lift and drag forces are conveniently expressed in the spar-carried coordinate frames, which can be transformed to the body frame. The aerodynamic forces associated with each wing and stroke expressed in both the spar and body frames are summarized in Table 1.

The center of pressure of a wing rotating about a fixed hinge line can be computed using blade-element theory [18]. The center of pressure of each wing can be conveniently expressed in the local wing planform frame associated with each stroke. To calculate the instantaneous center of pressure in the body frame, three coordinate frame rotations and one translation must be performed. The resulting expressions for the centers of pressure associated with each wing and stroke, expressed in the body frame, are summarized in Table 2. In these expressions, x_{cp}^{WP} and y_{cp}^{WP} are the x and y locations of the center of pressure in the local wing planform frame, Δr_R^B is defined as the position vector from the origin of the body frame to the origin of the right wing root coordinate system, i.e.,

$$\Delta r_R^B \triangleq \mathbf{r}_{o_{RW}}^B = \begin{bmatrix} \Delta x_R^B & \frac{w}{2} & \Delta z_R^B \end{bmatrix} \quad (19)$$

$$\Delta r_L^B \triangleq \mathbf{r}_{o_{LW}}^B = \begin{bmatrix} \Delta x_L^B & -\frac{w}{2} & \Delta z_L^B \end{bmatrix}$$

and the width of the vehicle is defined as w .

Table 1 Aerodynamic forces expressed in local spar and body frames

Force	Local spar frame	Body frame
RW upstroke	$\mathbf{F}_{RWU}^{RWS} = \begin{bmatrix} D_{RWU} \\ 0 \\ -L_{RWU} \end{bmatrix}$	$\mathbf{F}_{RWU}^B = \begin{bmatrix} L_{RWU} \\ -D_{RWU} \sin \phi_{RWU}(t) \\ D_{RWU} \cos \phi_{RWU}(t) \end{bmatrix}$
RW downstroke	$\mathbf{F}_{RWD}^{RWS} = \begin{bmatrix} -D_{RWD} \\ 0 \\ -L_{RWD} \end{bmatrix}$	$\mathbf{F}_{RWD}^B = \begin{bmatrix} L_{RWD} \\ D_{RWD} \sin \phi_{RWD}(t) \\ -D_{RWD} \cos \phi_{RWD}(t) \end{bmatrix}$
LW upstroke	$\mathbf{F}_{LWU}^{LWS} = \begin{bmatrix} -D_{LWU} \\ 0 \\ -L_{LWU} \end{bmatrix}$	$\mathbf{F}_{LWU}^B = \begin{bmatrix} L_{LWU} \\ D_{LWU} \sin \phi_{LWU}(t) \\ D_{LWU} \cos \phi_{LWU}(t) \end{bmatrix}$
LW downstroke	$\mathbf{F}_{LWD}^{LWS} = \begin{bmatrix} D_{LWD} \\ 0 \\ -L_{LWD} \end{bmatrix}$	$\mathbf{F}_{LWD}^B = \begin{bmatrix} L_{LWD} \\ -D_{LWD} \sin \phi_{LWD}(t) \\ -D_{LWD} \cos \phi_{LWD}(t) \end{bmatrix}$

Table 2 Centers of pressure expressed in body frame

CP location	Body frame expression
RW upstroke	$\mathbf{r}_{cpRWU}^B = \begin{bmatrix} x_{cp}^{WP} \sin \alpha + \Delta x_R^B \\ x_{cp}^{WP} \sin \phi_{RW} \cos \alpha + y_{cp}^{WP} \cos \phi_{RW} + \frac{w}{2} \\ -x_{cp}^{WP} \cos \phi_{RW} \cos \alpha + y_{cp}^{WP} \sin \phi_{RW} + \Delta z_R^B \end{bmatrix}$
RW downstroke	$\mathbf{r}_{cpRWD}^B = \begin{bmatrix} x_{cp}^{WP} \sin \alpha + \Delta x_R^B \\ -x_{cp}^{WP} \sin \phi_{RW} \cos \alpha + y_{cp}^{WP} \cos \phi_{RW} + \frac{w}{2} \\ x_{cp}^{WP} \cos \phi_{RW} \cos \alpha + y_{cp}^{WP} \sin \phi_{RW} + \Delta z_R^B \end{bmatrix}$
LW upstroke	$\mathbf{r}_{cpLWU}^B = \begin{bmatrix} x_{cp}^{WP} \sin \alpha + \Delta x_L^B \\ -x_{cp}^{WP} \sin \phi_{LW} \cos \alpha - y_{cp}^{WP} \cos \phi_{LW} - \frac{w}{2} \\ -x_{cp}^{WP} \cos \phi_{LW} \cos \alpha + y_{cp}^{WP} \sin \phi_{LW} + \Delta z_L^B \end{bmatrix}$
LW downstroke	$\mathbf{r}_{cpLWD}^B = \begin{bmatrix} x_{cp}^{WP} \sin \alpha + \Delta x_L^B \\ x_{cp}^{WP} \sin \phi_{LW} \cos \alpha - y_{cp}^{WP} \cos \phi_{LW} - \frac{w}{2} \\ x_{cp}^{WP} \cos \phi_{LW} \cos \alpha + y_{cp}^{WP} \sin \phi_{LW} + \Delta z_L^B \end{bmatrix}$

C. Aerodynamic Moments in Body Frame

The expressions for the aerodynamic moments associated with each wing and stroke are given by

$$\begin{aligned}\mathbf{M}_{\text{RWU}}^B &= \mathbf{r}_{\text{cpRWU}}^B \times \mathbf{F}_{\text{RWU}}^B & \mathbf{M}_{\text{RWD}}^B &= \mathbf{r}_{\text{cpRWD}}^B \times \mathbf{F}_{\text{RWD}}^B \\ \mathbf{M}_{\text{LWU}}^B &= \mathbf{r}_{\text{cpLWU}}^B \times \mathbf{F}_{\text{LWU}}^B & \mathbf{M}_{\text{LWD}}^B &= \mathbf{r}_{\text{cpLWD}}^B \times \mathbf{F}_{\text{LWD}}^B\end{aligned}\quad (20)$$

Carrying out the cross-product operations and substituting the values from Tables 1 and 2 into the expressions in Eq. (20) yields

$$\mathbf{M}_{\text{RWU}}^B = \begin{bmatrix} D_{\text{RWU}}[y_{\text{cp}}^{\text{WP}} + \frac{w}{2} \cos \phi_{\text{RW}} + \Delta z_R^B \sin \phi_{\text{RW}}] \\ \{L_{\text{RWU}}[y_{\text{cp}}^{\text{WP}} \sin \phi_{\text{RW}} + \Delta z_R^B] - D_{\text{RWU}} \Delta x_R^B \cos \phi_{\text{RW}} - [L_{\text{RWU}} \cos \alpha + D_{\text{RWU}} \sin \alpha] x_{\text{cp}}^{\text{WP}} \cos \phi_{\text{RW}}\} \\ \{-D_{\text{RWU}} \Delta x_R^B \sin \phi_{\text{RW}} - L_{\text{RWU}}[\frac{w}{2} + y_{\text{cp}}^{\text{WP}} \cos \phi_{\text{RW}}] - [L_{\text{RWU}} \cos \alpha + D_{\text{RWU}} \sin \alpha] x_{\text{cp}}^{\text{WP}} \sin \phi_{\text{RW}}\} \end{bmatrix} \quad (21)$$

$$\mathbf{M}_{\text{RWD}}^B = \begin{bmatrix} -D_{\text{RWD}}[y_{\text{cp}}^{\text{WP}} + \frac{w}{2} \cos \phi_{\text{RW}} + \Delta z_R^B \sin \phi_{\text{RW}}] \\ \{L_{\text{RWD}}[y_{\text{cp}}^{\text{WP}} \sin \phi_{\text{RW}} + \Delta z_R^B] + D_{\text{RWD}} \Delta x_R^B \cos \phi_{\text{RW}} + [L_{\text{RWD}} \cos \alpha + D_{\text{RWD}} \sin \alpha] x_{\text{cp}}^{\text{WP}} \cos \phi_{\text{RW}}\} \\ \{D_{\text{RWD}} \Delta x_R^B \sin \phi_{\text{RW}} - L_{\text{RWD}}[\frac{w}{2} + y_{\text{cp}}^{\text{WP}} \cos \phi_{\text{RW}}] + [L_{\text{RWD}} \cos \alpha + D_{\text{RWD}} \sin \alpha] x_{\text{cp}}^{\text{WP}} \sin \phi_{\text{RW}}\} \end{bmatrix} \quad (22)$$

$$\mathbf{M}_{\text{LWU}}^B = \begin{bmatrix} D_{\text{LWU}}[-y_{\text{cp}}^{\text{WP}} - \frac{w}{2} \cos \phi_{\text{LW}} - \Delta z_L^B \sin \phi_{\text{LW}}] \\ \{L_{\text{LWU}}[y_{\text{cp}}^{\text{WP}} \sin \phi_{\text{LW}} + \Delta z_L^B] - D_{\text{LWU}} \Delta x_L^B \cos \phi_{\text{LW}} - [L_{\text{LWU}} \cos \alpha + D_{\text{LWU}} \sin \alpha] x_{\text{cp}}^{\text{WP}} \cos \phi_{\text{LW}}\} \\ \{D_{\text{LWU}} \Delta x_L^B \sin \phi_{\text{LW}} + L_{\text{LWU}}[\frac{w}{2} + y_{\text{cp}}^{\text{WP}} \cos \phi_{\text{LW}}] + [L_{\text{LWU}} \cos \alpha + D_{\text{LWU}} \sin \alpha] x_{\text{cp}}^{\text{WP}} \sin \phi_{\text{LW}}\} \end{bmatrix} \quad (23)$$

$$\mathbf{M}_{\text{LWD}}^B = \begin{bmatrix} D_{\text{LWD}}[y_{\text{cp}}^{\text{WP}} + \frac{w}{2} \cos \phi_{\text{LW}} + \Delta z_L^B \sin \phi_{\text{LW}}] \\ \{L_{\text{LWD}}[y_{\text{cp}}^{\text{WP}} \sin \phi_{\text{LW}} + \Delta z_L^B] + D_{\text{LWD}} \Delta x_L^B \cos \phi_{\text{LW}} + [L_{\text{LWD}} \cos \alpha + D_{\text{LWD}} \sin \alpha] x_{\text{cp}}^{\text{WP}} \cos \phi_{\text{LW}}\} \\ \{-D_{\text{LWD}} \Delta x_L^B \sin \phi_{\text{LW}} + L_{\text{LWD}}[\frac{w}{2} + y_{\text{cp}}^{\text{WP}} \cos \phi_{\text{LW}}] - [L_{\text{LWD}} \cos \alpha + D_{\text{LWD}} \sin \alpha] x_{\text{cp}}^{\text{WP}} \sin \phi_{\text{LW}}\} \end{bmatrix} \quad (24)$$

Equations (21–24) provide the expressions for the instantaneous aerodynamic moments generated by each wing at any point in a wingbeat cycle in the body-axis coordinate frame.

IV. Cycle-Averaged Blade-Element Model

To calculate the cycle-averaged forces and moments produced by wings that follow a split-cycle position profile, it is necessary to evaluate numerous integrals. Many of the integrands are of the form $\cos(\cos \omega t)$ or $\sin(\cos \omega t)$ and have no indefinite integral solutions. These terms arise as a result of coordinate transformations between local and body coordinate frames, coupled with the fact that the time-varying wing position is defined in terms of cosine wave segments. Fortunately, definite integrals involving such functions exist over the intervals of interest for the present problem and can be derived from results presented in Gradshteyn and Ryzhik [21]. The solution to many of these definite integrals involves a Bessel function of the first kind, $J_1(\cdot)$, and a Struve function. The integrals involving Struve functions evaluate to zero over the limits of integration that arise in the formulation of this particular problem. For convenience, the solutions to the definite integrals that are required to compute the cycle-averaged forces and moments are provided below:

$$I_1 \triangleq \int_0^{\frac{\pi}{\omega-\delta}} \sin^2[(\omega-\delta)t] dt = \frac{\pi}{2(\omega-\delta)} \quad (25)$$

$$I_2 \triangleq \int_0^{\frac{\pi}{\omega-\delta}} \sin^2[(\omega-\delta)t] \sin(\cos[(\omega-\delta)t]) dt = 0 \quad (26)$$

$$I_3 \triangleq \int_0^{\frac{\pi}{\omega-\delta}} \sin^2[(\omega-\delta)t] \cos(\cos[(\omega-\delta)t]) dt = \frac{\pi J_1(1)}{(\omega-\delta)} \quad (27)$$

$$I_4 \triangleq \int_{\frac{\pi}{\omega-\delta}}^{\frac{2\pi}{\omega}} \sin^2[(\omega+\sigma)t + \xi] dt = \frac{\pi}{2(\omega+\sigma)} \quad (28)$$

$$I_5 \triangleq \int_{\frac{\pi}{\omega-\delta}}^{\frac{2\pi}{\omega}} \sin^2[(\omega+\sigma)t + \xi] \sin(\cos[(\omega+\sigma)t + \xi]) dt = 0 \quad (29)$$

$$I_6 \triangleq \int_{\frac{\pi}{\omega-\delta}}^{\frac{2\pi}{\omega}} \sin^2[(\omega+\sigma)t + \xi] \cos(\cos[(\omega+\sigma)t + \xi]) dt = \frac{\pi J_1(1)}{\omega+\sigma} \quad (30)$$

A. Cycle-Averaged Forces

In this section, expressions for cycle-averaged aerodynamic forces are derived and expressed in terms of the split-cycle waveform control input parameters that govern the wing kinematics and time invariant constants. The instantaneous forces are integrated with respect to time as each wing operates over an upstroke and downstroke.

1. X Force

Substituting the expression for the instantaneous x body force from Table 1 into Eq. (10) produces

$$\bar{X}_{\text{RW}}^B = \frac{\omega_{\text{RW}}}{2\pi} \left[\int_0^{\frac{\pi}{\omega_{\text{RW}}-\delta_{\text{RW}}}} L_{\text{RWU}}(t) dt + \int_{\frac{\pi}{\omega_{\text{RW}}-\delta_{\text{RW}}}}^{\frac{2\pi}{\omega_{\text{RW}}}} L_{\text{RWD}}(t) dt \right] \quad (31)$$

Substituting Eqs. (7), (8), and (16) into Eq. (31) and noting that the time-varying functions under the integral signs are of the form I_1 and I_4 as given by Eqs. (25) and (28), respectively, Eq. (31) can be written as

$$\bar{X}_{\text{RW}}^B = \frac{k_L \omega_{\text{RW}}}{2\pi} [(\omega_{\text{RW}} - \delta_{\text{RW}})^2 I_1 + (\omega_{\text{RW}} + \sigma_{\text{RW}})^2 I_4] \quad (32)$$

or simply

$$\bar{X}_{\text{RW}}^B = \frac{k_L \omega_{\text{RW}}}{4} (2\omega_{\text{RW}} - \delta_{\text{RW}} + \sigma_{\text{RW}}) \quad (33)$$

Following a similar procedure for the left wing, it can be shown that

$$\bar{X}_{\text{LW}}^B = \frac{k_L \omega_{\text{LW}}}{4} (2\omega_{\text{LW}} - \delta_{\text{LW}} + \sigma_{\text{LW}}) \quad (34)$$

Note that both \bar{X}_{RW}^B and \bar{X}_{LW}^B are positive quantities. At a hover condition, where the x body-axis is normal to the surface of the Earth, the forces produced by both wings act to counter the vehicle weight.

2. Y Force

To compute the cycle-averaged y body force for each wing, the expression for the instantaneous y body aerodynamic force from Table 1 is substituted into Eq. (10) to obtain

$$\begin{aligned}\bar{Y}_{\text{RW}}^B &= \frac{\omega_{\text{RW}}}{2\pi} \left[\int_0^{\frac{\pi}{\omega_{\text{RW}} - \delta_{\text{RW}}}} -D_{\text{RWU}}(t) \sin[\phi_{\text{RW}}(t)] dt \right. \\ &\quad \left. + \int_{\frac{\pi}{\omega_{\text{RW}} - \delta_{\text{RW}}}}^{\frac{2\pi}{\omega_{\text{RW}}}} D_{\text{RWD}}(t) \sin[\phi_{\text{RW}}(t)] dt \right] \end{aligned}\quad (35)$$

Substituting Eqs. (3), (4), (7), (8), and (16) into Eq. (35) and noting that the time-varying functions under the integral signs are of the form I_2 and I_5 as given by Eqs. (26) and (29), respectively, Eq. (35) becomes

$$\bar{Y}_{\text{RW}}^B = 0 \quad (36)$$

Following a similar procedure for the left wing, it can be shown that

$$\bar{Y}_{\text{LW}}^B = 0 \quad (37)$$

Physically, this result arises from the fact that over a single stroke, the component of drag, pointing in the y body direction, points in the positive direction for the same amount of time as it does in the negative direction and with the same magnitude.

3. Z Force

The calculation of the cycle-averaged force in the z body direction follows a similar procedure. Substituting the expression for the instantaneous z body aerodynamic force from Table 1 into Eq. (10) yields

$$\begin{aligned}\bar{Z}_{\text{RW}}^B &= \frac{\omega_{\text{RW}}}{2\pi} \left[\int_0^{\frac{\pi}{\omega_{\text{RW}} - \delta_{\text{RW}}}} D_{\text{RWU}}(t) \cos[\phi_{\text{RW}}(t)] dt \right. \\ &\quad \left. + \int_{\frac{\pi}{\omega_{\text{RW}} - \delta_{\text{RW}}}}^{\frac{2\pi}{\omega_{\text{RW}}}} -D_{\text{RWD}}(t) \cos[\phi_{\text{RW}}(t)] dt \right] \end{aligned}\quad (38)$$

Substituting Eqs. (3), (4), (7), (8), and (16) into Eq. (38) and noting that the time-varying functions under the integral signs are of the form I_3 and I_6 as given by Eqs. (27) and (30), respectively, Eq. (38) can be written as

$$\bar{Z}_{\text{RW}}^B = \frac{k_D \omega_{\text{RW}}}{2\pi} [(\omega_{\text{RW}} - \delta_{\text{RW}})^2 I_3 - (\omega_{\text{RW}} + \sigma_{\text{RW}})^2 I_6] \quad (39)$$

or simply

$$\bar{Z}_{\text{RW}}^B = \frac{-k_D J_1(1) \omega_{\text{RW}}}{2} (\delta_{\text{RW}} + \sigma_{\text{RW}}) \quad (40)$$

Following a similar procedure for the left wing, it can be shown that

$$\bar{Z}_{\text{LW}}^B = \frac{-k_D J_1(1) \omega_{\text{LW}}}{2} (\delta_{\text{LW}} + \sigma_{\text{LW}}) \quad (41)$$

The result for the z body-axis is important because it shows that nonzero cycle-averaged forces can be generated and used to induce fore and aft linear accelerations; motion that would not have been possible using temporally symmetric wingbeat motion alone.

B. Cycle-Averaged Moments

In this section, expressions for the cycle-averaged aerodynamic moments are derived. The cycle-averaged moments are later used in the development of a control law that requires an evaluation of the change in cycle-averaged moments with respect to a change in the control input variables.

1. Rolling Moment

The cycle-averaged x body moment can be written in terms of Eq. (10) as

$$\bar{M}_{x\text{RW}}^B = \frac{\omega_{\text{RW}}}{2\pi} \left[\int_0^{\frac{\pi}{\omega_{\text{RW}} - \delta_{\text{RW}}}} M_{x\text{RWU}}(t) dt + \int_{\frac{\pi}{\omega_{\text{RW}} - \delta_{\text{RW}}}}^{\frac{2\pi}{\omega_{\text{RW}}}} M_{x\text{RWD}}(t) dt \right] \quad (42)$$

Substituting Eqs. (3), (4), (7), (8), (16), (21), and (22) into Eq. (42) and noting that the integrals are of the form given in Eqs. (25–30), Eq. (42) can be written as

$$\begin{aligned}\bar{M}_{x\text{RW}}^B &= \frac{\omega_{\text{RW}} k_D}{2\pi} \left\{ (\omega_{\text{RW}} - \delta_{\text{RW}})^2 \left[y_{\text{cp}}^{\text{WP}} I_1 + \Delta z_R^B I_2 + \frac{w}{2} I_3 \right] \right. \\ &\quad \left. - (\omega_{\text{RW}} + \sigma_{\text{RW}})^2 \left[y_{\text{cp}}^{\text{WP}} I_4 + \Delta z_R^B I_5 + \frac{w}{2} I_6 \right] \right\} \end{aligned}\quad (43)$$

Substituting the results for the definite integrals I_1 – I_6 and simplifying yields

$$\bar{M}_{x\text{RW}}^B = -\frac{k_D \omega_{\text{RW}} (\delta_{\text{RW}} + \sigma_{\text{RW}})}{4} [y_{\text{cp}}^{\text{WP}} + w J_1(1)] \quad (44)$$

Following a similar procedure for the left wing, it can be shown that

$$\bar{M}_{x\text{LW}}^B = \frac{k_D \omega_{\text{LW}} (\delta_{\text{LW}} + \sigma_{\text{LW}})}{4} [y_{\text{cp}}^{\text{WP}} + w J_1(1)] \quad (45)$$

Note that without split-cycle frequency modulation, i.e., $\delta_{\text{RW}} = \sigma_{\text{RW}} = \delta_{\text{LW}} = \sigma_{\text{LW}} = 0$, it would not be possible to generate nonzero cycle-averaged rolling moments on this vehicle.

2. Pitching Moment

The instantaneous y body moment from Eq. (10) is

$$\bar{M}_{y\text{RW}}^B = \frac{\omega_{\text{RW}}}{2\pi} \left[\int_0^{\frac{\pi}{\omega_{\text{RW}} - \delta_{\text{RW}}}} M_{y\text{RWU}}(t) dt + \int_{\frac{\pi}{\omega_{\text{RW}} - \delta_{\text{RW}}}}^{\frac{2\pi}{\omega_{\text{RW}}}} M_{y\text{RWD}}(t) dt \right] \quad (46)$$

Substituting Eqs. (3), (4), (7), (8), (16), (21), and (22) into Eq. (46) and noting that the integrals are of the form given in Eqs. (25–30), Eq. (46) can be written as

$$\begin{aligned}\bar{M}_{y\text{RW}}^B &= \frac{\omega_{\text{RW}}}{2\pi} \left\{ (\omega_{\text{RW}} - \delta_{\text{RW}})^2 [k_L \Delta z_R^B I_1 - k_D \Delta x_R^B I_3 \right. \\ &\quad \left. - k_L x_{\text{cp}}^{\text{WP}} \cos \alpha I_3 - k_D x_{\text{cp}}^{\text{WP}} \sin \alpha I_3 + k_L y_{\text{cp}}^{\text{WP}} I_2] \right. \\ &\quad \left. + (\omega_{\text{RW}} + \sigma_{\text{RW}})^2 [k_L \Delta z_R^B I_4 + k_D \Delta x_R^B I_6 + k_L x_{\text{cp}}^{\text{WP}} \cos \alpha I_6 \right. \\ &\quad \left. + k_D x_{\text{cp}}^{\text{WP}} \sin \alpha I_6 + k_L y_{\text{cp}}^{\text{WP}} I_5] \right\} \end{aligned}\quad (47)$$

Substituting the results for the definite integrals I_1 – I_6 and simplifying produces

$$\begin{aligned}\bar{M}_{y\text{RW}}^B &= \frac{k_L \omega_{\text{RW}}}{2} \left[x_{\text{cp}}^{\text{WP}} J_1(1) \cos \alpha (\delta_{\text{RW}} + \sigma_{\text{RW}}) \right. \\ &\quad \left. + \frac{\Delta z_R^B}{2} (2\omega_{\text{RW}} + \sigma_{\text{RW}} - \delta_{\text{RW}}) \right] \\ &\quad + \frac{k_D J_1(1) \omega_{\text{RW}}}{2} \{(\delta_{\text{RW}} + \sigma_{\text{RW}})[x_{\text{cp}}^{\text{WP}} \sin \alpha + \Delta x_R^B]\} \end{aligned}\quad (48)$$

Following a similar procedure for the left wing, it can be shown that

$$\begin{aligned}\bar{M}_{y\text{LW}}^B &= \frac{k_L \omega_{\text{LW}}}{2} \left[x_{\text{cp}}^{\text{WP}} J_1(1) \cos \alpha (\delta_{\text{LW}} + \sigma_{\text{LW}}) \right. \\ &\quad \left. + \frac{\Delta z_L^B}{2} (2\omega_{\text{LW}} + \sigma_{\text{LW}} - \delta_{\text{LW}}) \right] \\ &\quad + \frac{k_D J_1(1) \omega_{\text{LW}}}{2} \{(\delta_{\text{LW}} + \sigma_{\text{LW}})[x_{\text{cp}}^{\text{WP}} \sin \alpha + \Delta x_L^B]\} \end{aligned}\quad (49)$$

Without split-cycle frequency modulation there still exists a nonzero cycle-averaged pitching moment if $\Delta z_R^B \neq 0$ or $\Delta z_L^B \neq 0$. This result

yields further insight into vehicle design for controllability. It suggests that the wing root hinge point should be placed such that its z body location is coincident with that of the nominal vehicle center of gravity, i.e., $\Delta z_R^B = 0$, $\Delta z_L^B = 0$. Such an arrangement will yield a zero cycle-averaged pitching moment when the split-cycle parameters are zero, which is a desirable feature for maintaining hover. Note that the current Harvard RoboFly aircraft does not incorporate this feature and would immediately pitch forward if not constrained by the guide wires used in their experiment [13]. Later, a bob-weight actuator is introduced that can be used to manipulate pitching moments using mechanical, rather than aerodynamic, means.

3. Yawing Moment

Expressions for the cycle-averaged aerodynamic moments in the z body frame will now be derived. Substituting the expression for the instantaneous z body moment into Eq. (10) yields

$$\overline{M}_z^B_{RW} = \frac{\omega_{RW}}{2\pi} \left[\int_0^{\frac{\pi}{\omega_{RW}-\delta_{RW}}} M_{zRWU}(t) dt + \int_{\frac{\pi}{\omega_{RW}-\delta_{RW}}}^{\frac{2\pi}{\omega_{RW}}} M_{zRWD}(t) dt \right] \quad (50)$$

Substituting Eqs. (3), (4), (7), (8), (16), (21), and (22) into Eq. (50) and noting that the integrals are of the form given in Eqs. (25–30), Eq. (50) can be written as

$$\begin{aligned} \overline{M}_z^B_{RW} = & \frac{\omega_{RW}}{2\pi} \left\{ (\omega_{RW} - \delta_{RW})^2 \left[-k_L \frac{w}{2} I_1 - k_D \Delta x_R^B I_2 - k_L y_{cp}^{WP} I_3 \right. \right. \\ & - k_L x_{cp}^{WP} \cos \alpha I_2 - k_D x_{cp}^{WP} \sin \alpha I_2 \left. \right] + (\omega_{RW} + \sigma_{RW})^2 \left[-k_L \frac{w}{2} I_4 \right. \\ & \left. + k_D \Delta x_R^B I_5 - k_L y_{cp}^{WP} I_6 + k_L x_{cp}^{WP} \cos \alpha I_5 + k_D x_{cp}^{WP} \sin \alpha I_5 \right] \right\} \end{aligned} \quad (51)$$

Substituting the results for the definite integrals I_1 – I_6 and simplifying yields

$$\overline{M}_z^B_{RW} = \frac{-k_L \omega_{RW}}{2} \left[\left(y_{cp}^{WP} J_1(1) + \frac{w}{4} \right) (2\omega_{RW} - \delta_{RW} + \sigma_{RW}) \right] \quad (52)$$

Following a similar procedure for the left wing, it can be shown that

$$\overline{M}_z^B_{LW} = \frac{k_L \omega_{LW}}{2} \left[\left(y_{cp}^{WP} J_1(1) + \frac{w}{4} \right) (2\omega_{LW} - \delta_{LW} + \sigma_{LW}) \right] \quad (53)$$

Without split-cycle frequency modulation, there exists a nonzero cycle-averaged yawing moment on each wing since $y_{cp}^{WP} \neq 0$ and $w \neq 0$. When the split-cycle parameters for each wing are zero, the cycle-averaged moments are opposing and balance one another. Since the fundamental or symmetric wingbeat frequency can be independently varied for each wing, yawing moments can be generated without varying the split-cycle parameters.

V. Control Derivatives

The parameters used to control the aerodynamic force and moment profiles are the fundamental wingbeat frequencies ω_{RW} and ω_{LW} and the split-cycle parameters δ_{RW} and δ_{LW} . For controllability analysis and control synthesis, the sensitivity of each cycle-averaged generalized force to each control input parameter is determined.

The partial derivatives of each cycle-averaged force and moment with respect to each aerodynamic control input parameter can be calculated by differentiating Eqs. (33), (34), (36), (37), (40), (41), (44), (45), (48), (49), (52), and (53) and the full expressions for these control derivatives are presented in Oppenheimer et al. [19]. Here, the control of the proposed aircraft in the vicinity of hover is of interest; therefore, the only the control derivatives at the hover condition where $\omega_{RW} = \omega_{LW} = \omega_o$ and $\delta_{RW} = \delta_{LW} = 0$ are presented. Expressions relating the hover frequency to the wing

geometry, lift coefficient, and mass have been published [9,12] and the expression derived by Doman et al. [12] is used here:

$$\omega_o = \sqrt{\frac{2 mg}{\rho I_A C_L(\alpha)}} \quad (54)$$

This condition assumes that there are two wings flapping symmetrically left to right, i.e., $\omega_{RW} = \omega_{LW}$ and $\delta_{RW} = \delta_{LW} = 0$, and that the angular position of each wing in the stroke plane is defined by $\phi(t) = \cos(\omega_o t)$. Also, it is assumed that the nominal center of gravity of the vehicle and wing root hinges are aligned such that $\Delta z_R^B = \Delta z_L^B = 0$. The control derivatives about hover are presented in Table 3. Note that for $\Delta z_R^B = \Delta z_L^B = 0$, $\frac{\partial \overline{M}_z^B}{\partial \omega_{RW}}|_{\omega_{RW}=\omega_o, \delta_{RW}=0} = 0$ and $\frac{\partial \overline{M}_z^B}{\partial \omega_{LW}}|_{\omega_{LW}=\omega_o, \delta_{LW}=0} = 0$.

A. Bob-Weight Control Derivatives

Using only the aerodynamic control input parameters, changes in pitching moment are accompanied by undesirable changes in other forces and moments. It is for this reason that a bob-weight actuator has been introduced. The bob-weight should lie in the vehicle plane of symmetry and at zero deflection should be coincident with the undeflected center of gravity. The bob-weight need not be dead weight. Any necessary vehicle component that is not sensitive to movement could serve the purpose, e.g., battery, power converter, etc. The weight would be mounted near the tip of a bimorph piezoelectric actuator. The tip deflection would primarily consist of translation in the z body-axis direction, while translation in the x body direction would be so small as to be negligible. Hence, the bob-weight motion is in the x_B , z_B plane.

Let m_o be the total vehicle mass exclusive of the bob-weight and bob-weight actuator and $x_{cg_o}^B$, $0, z_{cg_o}^B$ be the location of the center of mass, in body coordinates, of only the vehicle. Let m_{BW} denote the mass of the bob-weight and actuator assembly and $x_{BW}^B, 0, z_{BW}^B$ be the location of the center of mass of this assembly in body coordinates. Because of the nature of the tip motion of the bimorph actuator, it is assumed that motion of the bob-weight does not alter the x location of the center of mass of the bob-weight assembly; hence, x_{BW}^B is a

Table 3 Aerodynamic control derivatives about hover

Control derivative $\frac{\partial \overline{G}}{\partial \alpha} _{\omega=\omega_o, \delta=0}$
$\frac{\partial \overline{F}_{xRW}^B}{\partial \delta_{RW}} _{\omega_{RW}=\omega_o, \delta_{RW}=0} = \frac{\partial \overline{F}_{xLW}^B}{\partial \delta_{LW}} _{\omega_{LW}=\omega_o, \delta_{LW}=0} = 0$
$\frac{\partial \overline{F}_{yRW}^B}{\partial \delta_{RW}} _{\omega_{RW}=\omega_o, \delta_{RW}=0} = \frac{\partial \overline{F}_{yLW}^B}{\partial \delta_{LW}} _{\omega_{LW}=\omega_o, \delta_{LW}=0} = k_L \omega_o$
$\frac{\partial \overline{F}_{zRW}^B}{\partial \delta_{RW}} _{\omega_{RW}=\omega_o, \delta_{RW}=0} = \frac{\partial \overline{F}_{zLW}^B}{\partial \delta_{LW}} _{\omega_{LW}=\omega_o, \delta_{LW}=0} = 0$
$\frac{\partial \overline{F}_{xRW}^B}{\partial \delta_{RW}} _{\omega_{RW}=\omega_o, \delta_{RW}=0} = \frac{\partial \overline{F}_{xLW}^B}{\partial \delta_{LW}} _{\omega_{LW}=\omega_o, \delta_{LW}=0} = 0$
$\frac{\partial \overline{F}_{yRW}^B}{\partial \delta_{RW}} _{\omega_{RW}=\omega_o, \delta_{RW}=0} = -k_D J_1(1) \omega_o$
$\frac{\partial \overline{F}_{zRW}^B}{\partial \delta_{RW}} _{\omega_{RW}=\omega_o, \delta_{RW}=0} = \frac{\partial \overline{F}_{zLW}^B}{\partial \delta_{LW}} _{\omega_{LW}=\omega_o, \delta_{LW}=0} = 0$
$\frac{\partial \overline{F}_{xLW}^B}{\partial \delta_{LW}} _{\omega_{LW}=\omega_o, \delta_{LW}=0} = -k_D J_1(1) \omega_o$
$\frac{\partial \overline{M}_{zRW}^B}{\partial \delta_{RW}} _{\omega_{RW}=\omega_o, \delta_{RW}=0} = -\frac{1}{2} k_D \omega_o (y_{cp}^{WP} + w J_1(1))$
$\frac{\partial \overline{M}_{zLW}^B}{\partial \delta_{LW}} _{\omega_{LW}=\omega_o, \delta_{LW}=0} = \frac{\partial \overline{M}_{zLW}^B}{\partial \omega_{LW}} _{\omega_{LW}=\omega_o, \delta_{LW}=0} = 0$
$\frac{\partial \overline{M}_{zRW}^B}{\partial \delta_{LW}} _{\omega_{RW}=\omega_o, \delta_{LW}=0} = \frac{1}{2} k_D \omega_o (y_{cp}^{WP} + w J_1(1))$
$\frac{\partial \overline{M}_{zLW}^B}{\partial \delta_{RW}} _{\omega_{LW}=\omega_o, \delta_{RW}=0} = J_1(1) \omega_o [k_L x_{cp}^{WP} \cos \alpha + k_D (x_{cp}^{WP} \sin \alpha + \Delta x_R^B)]$
$\frac{\partial \overline{M}_{zRW}^B}{\partial \omega_{RW}} _{\omega_{RW}=\omega_o, \delta_{RW}=0} = k_L \Delta z_R^B \omega_o$
$\frac{\partial \overline{M}_{zLW}^B}{\partial \delta_{LW}} _{\omega_{LW}=\omega_o, \delta_{LW}=0} = J_1(1) \omega_o [k_L x_{cp}^{WP} \cos \alpha + k_D (x_{cp}^{WP} \sin \alpha + \Delta x_L^B)]$
$\frac{\partial \overline{M}_{zLW}^B}{\partial \omega_{LW}} _{\omega_{LW}=\omega_o, \delta_{LW}=0} = k_L \Delta z_L^B \omega_o$
$\frac{\partial \overline{M}_{zRW}^B}{\partial \delta_{LW}} _{\omega_{RW}=\omega_o, \delta_{LW}=0} = \frac{\partial \overline{M}_{zLW}^B}{\partial \delta_{LW}} _{\omega_{LW}=\omega_o, \delta_{LW}=0} = 0$
$\frac{\partial \overline{M}_{zLW}^B}{\partial \omega_{RW}} _{\omega_{RW}=\omega_o, \delta_{RW}=0} = -2k_L \omega_o [y_{cp}^{WP} J_1(1) + \frac{w}{4}]$
$\frac{\partial \overline{M}_{zLW}^B}{\partial \omega_{LW}} _{\omega_{LW}=\omega_o, \delta_{LW}=0} = 2k_L \omega_o [y_{cp}^{WP} J_1(1) + \frac{w}{4}]$

constant. Defining x_{cg}^B , 0 , z_{cg}^B as the location of the center of mass of the entire vehicle, including the bob-weight, this assumption implies that x_{cg}^B is fixed for a given bob-weight mass. Wood [13] indicates that the mass of each wing is less than 1% of the gross vehicle weight; therefore, it is also assumed that the mass of each wing is negligible. Under the above conditions, the x and z body locations of the center of mass are given by

$$x_{cg}^B = \frac{x_{cg_o}^B m_o + x_{BW}^B m_{BW}}{m_o + m_{BW}} \quad (55)$$

$$z_{cg}^B = \frac{z_{cg_o}^B m_o + z_{BW}^B m_{BW}}{m_o + m_{BW}} \quad (56)$$

It is important to note that the moments produced by aerodynamic forces are taken about the body frame and are independent of the center-of-mass location, even when the center of mass is not coincident with the origin of the body-axes system. Therefore, the moments about the body axes are composed of aerodynamic moments and moments due to center-of-mass offset. In other words, the total cycle-averaged moments about the body-axes coordinate system $\bar{\mathbf{M}}^B$ become

$$\bar{\mathbf{M}}^B = \bar{\mathbf{M}}_{aero}^B + \bar{\mathbf{M}}_{cg}^B \quad (57)$$

where $\bar{\mathbf{M}}_{aero}^B$ is the cycle-averaged moment produced by lift and drag of the wings and $\bar{\mathbf{M}}_{cg}^B$ is the cycle-averaged moment due to center-of-mass offset from the origin of the body axes. The cycle-averaged moment due to center-of-mass offset is

$$\bar{\mathbf{M}}_{cg}^B = \frac{\omega}{2\pi} \int_0^{2\pi} \mathbf{r}_{cg}^B \times \mathbf{F}_{cg}^B dt \quad (58)$$

where the integral of each component of the integrand is evaluated, $\mathbf{r}_{cg}^B = [x_{cg}^B \ 0 \ z_{cg}^B]$ is the position vector from the center of mass to the origin of the body axes, and x_{cg}^B , z_{cg}^B are provided in Eqs. (55) and (56). The force in Eq. (58) is gravitational and can be written as

$$\mathbf{F}_{cg}^B = \mathbf{R}_I^B [- (m_o + m_{BW})g \ 0 \ 0] \quad (59)$$

where \mathbf{R}_I^B is a rotation matrix from the inertial frame to the body frame and g is the acceleration due to gravity. Let this force, in general, be represented as $\mathbf{F}_{cg}^B = [F_{x_{cg}}^B \ F_{y_{cg}}^B \ F_{z_{cg}}^B]$. Then, by

$$\begin{bmatrix} \Delta \bar{F}_{x_{com}}^B \\ \Delta \bar{F}_{y_{com}}^B \\ \Delta \bar{F}_{z_{com}}^B \\ \Delta \bar{M}_{x_{com}}^B \\ \Delta \bar{M}_{y_{com}}^B \\ \Delta \bar{M}_{z_{com}}^B \end{bmatrix} = \begin{bmatrix} 0 & B_{12} & 0 & B_{14} & 0 \\ 0 & 0 & 0 & 0 & 0 \\ -k_D J_1(1) \omega_o & 0 & -k_D J_1(1) \omega_o & 0 & 0 \\ -\frac{1}{2} k_D \omega_o (y_{cp}^{WP} + w J_1(1)) & 0 & \frac{1}{2} k_D \omega_o (y_{cp}^{WP} + w J_1(1)) & 0 & B_{45} \\ B_{51} & 0 & B_{53} & 0 & B_{55} \\ 0 & B_{62} & 0 & B_{64} & 0 \end{bmatrix} \begin{bmatrix} \delta_{RW} \\ \Delta \omega_{RW} \\ \delta_{LW} \\ \Delta \omega_{LW} \\ V_{BW} \end{bmatrix}$$

performing the cross-product operation, the moment due to center-of-mass offset is

$$\bar{\mathbf{M}}_{cg}^B = \frac{\omega}{2\pi} \int_0^{2\pi} \begin{bmatrix} -z_{cg}^B F_{y_{cg}}^B \\ z_{cg}^B F_{x_{cg}}^B - x_{cg}^B F_{z_{cg}}^B \\ x_{cg}^B F_{y_{cg}}^B \end{bmatrix} dt \quad (60)$$

If the position vector \mathbf{r}_{cg}^B and the force in Eq. (59) are constant over a full wingbeat cycle, then Eq. (60) becomes

$$\bar{\mathbf{M}}_{cg}^B = \begin{bmatrix} -z_{cg}^B F_{y_{cg}}^B \\ z_{cg}^B F_{x_{cg}}^B - x_{cg}^B F_{z_{cg}}^B \\ x_{cg}^B F_{y_{cg}}^B \end{bmatrix} \quad (61)$$

It is assumed that a linear relationship exists between the bob-weight control voltage applied to the actuator, V_{BW} , and the bob-weight tip deflection:

$$\frac{\partial z_{BW}^B}{\partial V_{BW}} = k_{BW} \quad (62)$$

Additionally, x_{BW}^B is taken to be constant; therefore, $\frac{\partial x_{BW}^B}{\partial V_{BW}} = 0$; thus, the control effectiveness of the bob-weight can be expressed as

$$\frac{\partial \bar{\mathbf{M}}_{cg}^B}{\partial V_{BW}} = \frac{\partial \bar{\mathbf{M}}_{cg}^B}{\partial z_{BW}^B} \frac{\partial z_{BW}^B}{\partial V_{BW}} \quad (63)$$

Substituting Eq. (56) into Eq. (61) and computing the derivatives as specified in Eq. (63) yields

$$\frac{\partial \bar{\mathbf{M}}_{cg}^B}{\partial V_{BW}} = \begin{pmatrix} \frac{-m_{BW}}{m_o + m_{BW}} F_{y_{cg}}^B k_{BW} \\ \frac{m_{BW}}{m_o + m_{BW}} F_{x_{cg}}^B k_{BW} \\ 0 \end{pmatrix} \quad (64)$$

For flight near hover, $F_{x_{cg}}^B \gg F_{y_{cg}}^B$ because both the vehicle pitch and yaw attitudes stay near 0 deg.

B. Control Effectiveness

The final form of the control-oriented model consists of a cycle-averaged blade-element model that is linearized about hover. Within this framework, a linear relationship exists between the cycle-averaged force and moment commands generated by a conventional feedback control law and the control parameters. Letting \bar{G} denote a generalized force or moment, the total increment of commanded \bar{G} is

$$\Delta \bar{G}_{com} = \frac{\partial \bar{G}}{\partial \delta_{RW}} \delta_{RW} + \frac{\partial \bar{G}}{\partial \omega_{RW}} \Delta \omega_{RW} + \frac{\partial \bar{G}}{\partial \delta_{LW}} \delta_{LW} + \frac{\partial \bar{G}}{\partial \omega_{LW}} \Delta \omega_{LW} + \frac{\partial \bar{G}}{\partial V_{BW}} V_{BW} \quad (65)$$

Writing this expression for the three forces and three moments produces

$$\begin{bmatrix} \Delta \bar{F}_{x_{com}}^B \\ \Delta \bar{F}_{y_{com}}^B \\ \Delta \bar{F}_{z_{com}}^B \\ \Delta \bar{M}_{x_{com}}^B \\ \Delta \bar{M}_{y_{com}}^B \\ \Delta \bar{M}_{z_{com}}^B \end{bmatrix} = \mathbf{B}_A \begin{bmatrix} \delta_{RW} \\ \Delta \omega_{RW} \\ \delta_{LW} \\ \Delta \omega_{LW} \\ V_{BW} \end{bmatrix} \quad (66)$$

where \mathbf{B}_A is the control effectiveness matrix. The elements of this matrix are the sensitivities of the cycle-averaged forces and moments to changes in control input variations that are presented in Table 3 and Eq. (64). Also,

$$\begin{aligned} B_{12} &= B_{14} = k_L \omega_o & B_{62} &= -B_{64} = -2k_L \omega_o \left[y_{cp}^{WP} J_1(1) + \frac{w}{4} \right] \\ B_{51} &= J_1(1) \omega_o [k_L x_{cp}^{WP} \cos \alpha + k_D (x_{cp}^{WP} \sin \alpha + \Delta x_R^B)] & B_{53} &= J_1(1) \omega_o [k_L x_{cp}^{WP} \cos \alpha + k_D (x_{cp}^{WP} \sin \alpha + \Delta x_L^B)] \\ B_{45} &= -k_{BW} \left(\frac{m_{BW}}{m_o + m_{BW}} \right) F_{y_{cg}}^B & B_{55} &= k_{BW} \left(\frac{m_{BW}}{m_o + m_{BW}} \right) F_{x_{cg}}^B \end{aligned} \quad (67)$$

A feedback control law, discussed shortly, generates the cycle-averaged force and moment commands that form the left-hand side of

Eq. (66). The control allocation objective is to find the control input vector $[\delta_{RW} \Delta\omega_{RW} \delta_{LW} \Delta\omega_{LW} V_{BW}]^T$, such that Eq. (66) is satisfied.

Examination of this matrix reveals what can be achieved by manipulating the four parameters that define the motion of the wings and the bob-weight. The rank of this matrix is five. Most obviously, it is not possible to generate direct side forces on the vehicle using the five control parameters. The next observation is that rows associated with the z force and pitching moment would be linearly dependent for $\Delta z_R^B = \Delta z_L^B = 0$ and $\Delta x_R^B = \Delta x_L^B$ if it were not for the presence of the bob-weight actuator. These conditions would exist on a well designed vehicle because of the existence of a plane of symmetry and the fact that, from a vehicle design perspective, it is desirable that the z offset between the nominal center of gravity and the wing root hinge points be zero. Such an arrangement eliminates a source of undesirable pitching moments associated with ω_o that would tend to destabilize the hover condition unless active control were applied. The sparsity of the control effectiveness matrix shows that the split-cycle method provides a high degree of input decoupling, which simplifies control allocation. The analytic formulation allows for a great deal of insight into the physics of the control problem, which can aid in the design of the controller as well as the vehicle itself [19].

VI. Equations of Motion

A standard set of 6-degree-of-freedom rigid body equations of motion are employed [22]. These are the same equations that describe the motion of a rigid body aircraft; however, because the angle of each wing in the stroke plane is a periodic function of time, the forces and moments that drive the equations consist of multiple, independent, and variable periodic functions of time. It is assumed that the wings are massless; therefore, there exists no inertial coupling between the fuselage and the wings. It is hypothesized that the inertial coupling between the wings and body will be small because in the Harvard Robofly the wings constitute less than 1% of the total vehicle weight [13]. The equations of motion are

$$\begin{bmatrix} \dot{p} \\ \dot{q} \\ \dot{r} \end{bmatrix} = \mathbf{I}^{-1}(\mathbf{M}^B(t) - \boldsymbol{\omega} \times \mathbf{I}\boldsymbol{\omega}) \quad (68)$$

$$\begin{bmatrix} \dot{u} \\ \dot{v} \\ \dot{w} \end{bmatrix} = \begin{bmatrix} qw - rv \\ ru - pw \\ pv - qu \end{bmatrix} + \frac{1}{m}[\mathbf{F}^B(t)] - \mathbf{R}_I^B \begin{bmatrix} 0 \\ 0 \\ -g \end{bmatrix} \quad (69)$$

$$\begin{bmatrix} \dot{x} \\ \dot{y} \\ \dot{z} \end{bmatrix} = \mathbf{R}_B^I \begin{bmatrix} u \\ v \\ w \end{bmatrix} \quad (70)$$

$$\begin{bmatrix} \dot{q}_0 \\ \dot{q}_1 \\ \dot{q}_2 \\ \dot{q}_3 \end{bmatrix} = \begin{bmatrix} 0 & -p & -q & -r \\ p & 0 & r & -q \\ q & -r & 0 & p \\ r & q & -p & 0 \end{bmatrix} \begin{bmatrix} q_0 \\ q_1 \\ q_2 \\ q_3 \end{bmatrix} \quad (71)$$

where \mathbf{I} is the inertia matrix; $\boldsymbol{\omega} = [p \ q \ r]$ is the angular rate vector; $\mathbf{M}^B(t)$ is the sum of the left and right wing instantaneous aerodynamic moment vectors consisting of the rolling, pitching, and yawing moments; u , v , and w are the translational velocities; $\mathbf{F}^B(t)$ is sum of the left and right wing instantaneous aerodynamic force vectors; m is the vehicle mass; g is the acceleration due to gravity; x , y , and z are the vehicle positions with respect to an inertial frame; and $\mathbf{q} = q_0 + q_1\hat{i} + q_2\hat{j} + q_3\hat{k}$ is a quaternion used to perform the 3-2-1 standard Euler transformation. Also, $\mathbf{R}_B^I = \mathbf{R}_I^{B^T}$ are rotation matrices that transform from body to inertial axes and back.

A. Blade-Element Simulation

A low-fidelity blade-element-based model of the instantaneous aerodynamic forces and moments is used to drive equations of

motion in the first simulation model. These instantaneous forces and moments were presented earlier in Table 1 and Eqs. (21–24). This model does not account for leading-edge vortex and wake-capture effects that have been observed in experiments. The purpose of this simulation model is to assess the efficacy of the cycle-averaged control law when applied to a vehicle model that includes time periodic variations in the forces and moments due to the flapping wings.

B. Unsteady Aerodynamic Simulation

Unsteady aerodynamic phenomena can have a significant influence upon the instantaneous forces and moments produced by flapping wings at low Reynolds numbers. Significant discrepancies between the instantaneous aerodynamic forces predicted by blade-element theory and experimental measurements have been observed; however, it has been found that in a cycle-averaged sense, blade-element theory provides a reasonable prediction of cycle-averaged lift [20]. Blade-element theory has been found to underpredict cycle-averaged drag when compared with experimental measurements. Since the cycle-averaged control law is based on the sensitivities of cycle-averaged lift and drag with respect to the adjustable wing kinematic parameters and not the actual magnitudes of the forces, it is natural to ask whether the cycle-averaged blade-element model used to derive the control laws captures these sensitivities with sufficient fidelity to provide a reasonable level of closed-loop stability and tracking performance. To address this question, the fidelity of the aerodynamic forces produced by the flapping-wing vehicle model is increased by making use of the experimental results produced by Sane and Dickinson [20]. The experimental results were used to produce time-varying lift- and drag-coefficient profiles that provide a more complete representation of the forces and moments produced by a flapping wing at low Reynolds numbers. This representation not only includes translational and rotational contributions to the forces that can be predicted by quasi-steady methods, but also includes contributions from unsteady leading-edge vortex and wake interaction effects.

The lift and drag profiles for a given stroke and angle-of-attack profile are extracted from measurement time histories. The corresponding instantaneous aerodynamic coefficients were computed to form a look-up table. The computation of the coefficient tables is performed using the parameters of the flapping-wing system employed by Sane and Dickinson [20], while the computations of the aerodynamic forces in the simulation model used for this study use the parameters of the proposed flapping-wing MAV. The lift and drag force measured in the Sane and Dickinson experiment were observed for a 90 deg stroke amplitude with a symmetric flip of the wing, about the spar axis, that occurred in the vicinity of wing stroke reversals [20]. The measurement-based data was approximated by producing 1000-point look-up tables for lift and drag coefficients and for angle of attack, using constant interval sampling of the phase of the stroke. The phase of the stroke waveform is used as an index to extract data from the resulting aerodynamic coefficient tables. The angle of attack is also obtained from a look-up table that corresponds to the set of force coefficients being used. The angle-of-attack table is necessary because the instantaneous values of the aerodynamic coefficients depend upon the instantaneous angle-of-attack profile. The appropriate rotational angle is therefore produced to transform the lift and drag forces in the spar frame to the body frame. A comparison of the unsteady table look-up model to the instantaneous blade-element and cycle-averaged blade-element models for a sinusoidal velocity profile, i.e. $\omega_{RW} = \omega_{LW} = \omega_o$ and $\delta_{RW} = \delta_{LW} = 0$, is shown in Fig. 5. It can be seen that the instantaneous blade-element model underpredicts drag but captures the magnitude of the instantaneous lift rather well. The cycle-averaged blade-element model used for the model-based control design differs significantly from both the instantaneous blade-element and unsteady aerodynamic model over the course of the wingbeat; however, the controller is designed to control the low-frequency behavior of the fuselage, which is well below the wingbeat frequency.

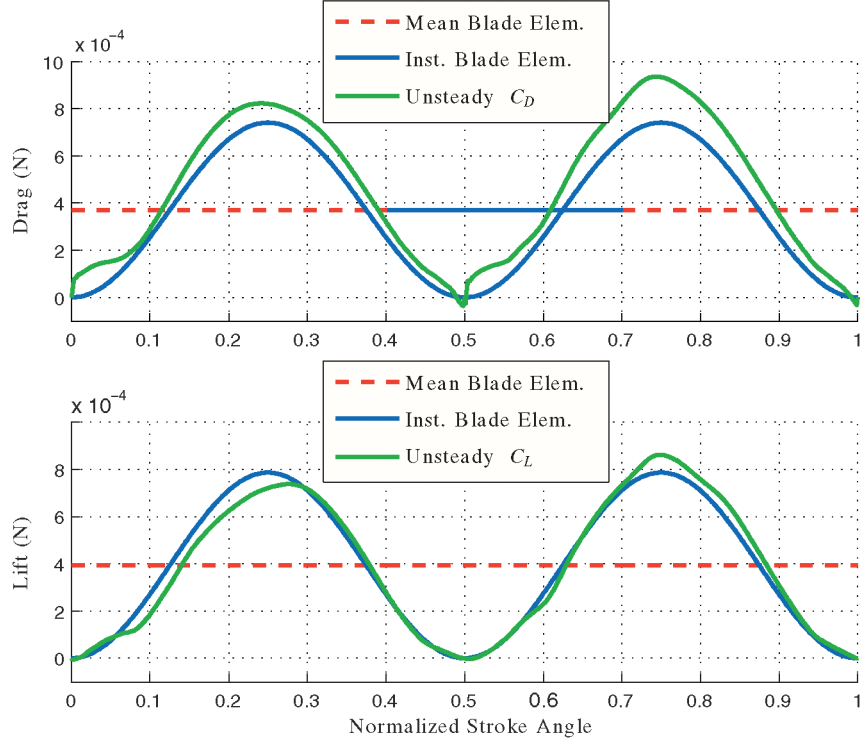


Fig. 5 Aerodynamic model comparison for temporally symmetric wingbeat.

In summary, the unsteady model relaxes the following assumptions used in the derivation of the control-oriented model: the two-dimensional sectional aerodynamic coefficients are known and constant throughout each stroke, and the passive wing rotation joint is on a limit when the wing angular velocity in the stroke plane is nonzero. The first assumption is replaced with a model where the aerodynamic coefficients of each wing are known, but vary as a function of angular position in the stroke plane. The second assumption is replaced by a model where the angle of attack smoothly varies as the wing moves through the stroke plane.

VII. Inner-Loop Control

The objective of the inner-loop controller is to render a neighborhood of a given point and orientation attractive. Seeking zero-error tracking to a fixed point and orientation is not possible because of the inherent periodic forcing of the system that results from the flapping wings. The control strategy is to use the available analytical expressions for wingbeat cycle-averaged forces and moments as a control-oriented model and consider the averaged forces and moments as virtual control inputs. The controller, therefore, assigns the wingbeat parameters for each cycle; thus, the output of the controller need only be computed once per wingbeat. Analysis of the cycle-averaged forces and moments shows that using a combination of left and right fundamental frequencies, split-cycle parameters, and bob-weight shifting yields control authority over all but the cycle-averaged side force. Hence, the controller will be a five-DOF controller, but it is expected to perform six-DOF tracking tasks.

The position, velocity, attitude, and angular velocities of the body are assumed to be available for feedback. They are used to compute an error between the vehicle state and a desired point and orientation. The high degree of input decoupling present in the control matrix \mathbf{B}_A enables the use of a simplistic feedback gain structure where the approach is to enforce a second-order response in each degree of freedom, considering each force and moment separately. The output of the feedback gains is the desired cycle-averaged forces and moments and forms the left-hand side of Eq. (66). Finally, control allocation is used to compute the wingbeat parameters, where the allocation is based on the control derivatives derived from the

analytic expressions for the wingbeat cycle-averaged forces and moments.

A. Error Computation

The error computation employs a given reference position and orientation, expressed with respect to the inertial coordinate frame. The error is expressed in body coordinates, transformed appropriately from the difference between the reference and the state of the vehicle. The feedback gain structure is based on considering each degree of freedom separately in the body coordinate frame, because expressions for the average forces and moments are available in the body frame. Computing the error in body frame coordinates is therefore consistent with the desired feedback gain structure. The velocity error can be computed similarly, when the reference is allowed to vary. The angular velocity error is approximated by the angular velocity of the vehicle in body coordinates. For a fixed reference orientation, no approximation is needed.

A desired position \mathbf{x}_d^I and a desired orientation defined by the Euler angles Φ_d^D are given, where D denotes the desired body frame. Alternatively, the reference orientation is represented by the rotation matrix \mathbf{R}_d^D from the inertial frame to the desired frame. The tracking error is computed as

$$\begin{aligned} \mathbf{x}_e^B &= \mathbf{R}_d^B(\mathbf{x}^I - \mathbf{x}_d^I) & \mathbf{v}_e^B &= \dot{\mathbf{x}}^B - \mathbf{R}_d^B(\dot{\mathbf{x}}_d^I) & \mathbf{R}_D^B &= \mathbf{R}_d^B(\mathbf{R}_d^D)^T \\ & & & & & \omega_e^B = (p \ q \ r)^T \end{aligned} \quad (72)$$

where $\mathbf{x}_e^B = (x_e \ y_e \ z_e)^T$ is the position error, $\mathbf{v}_e^B = (\dot{x}_e^B \ \dot{y}_e^B \ \dot{z}_e^B)^T$ is the velocity error, \mathbf{R}_D^B is the rotation matrix from the desired frame to the body frame, and $\omega_e^B = (p_e \ q_e \ r_e)^T$ is the angular velocity error. A vector of Euler angle tracking errors $[\phi_e \ \theta_e \ \psi_e]^T$ can be derived from the \mathbf{R}_D^B rotation matrix using standard methods [23].

B. Feedback Gain Structure

The feedback controller is based upon the simplistic view of treating each degree of freedom separately. This is possible because of the use of a control allocator that translates cycle-averaged generalized force commands into wingbeat oscillator and bob-weight

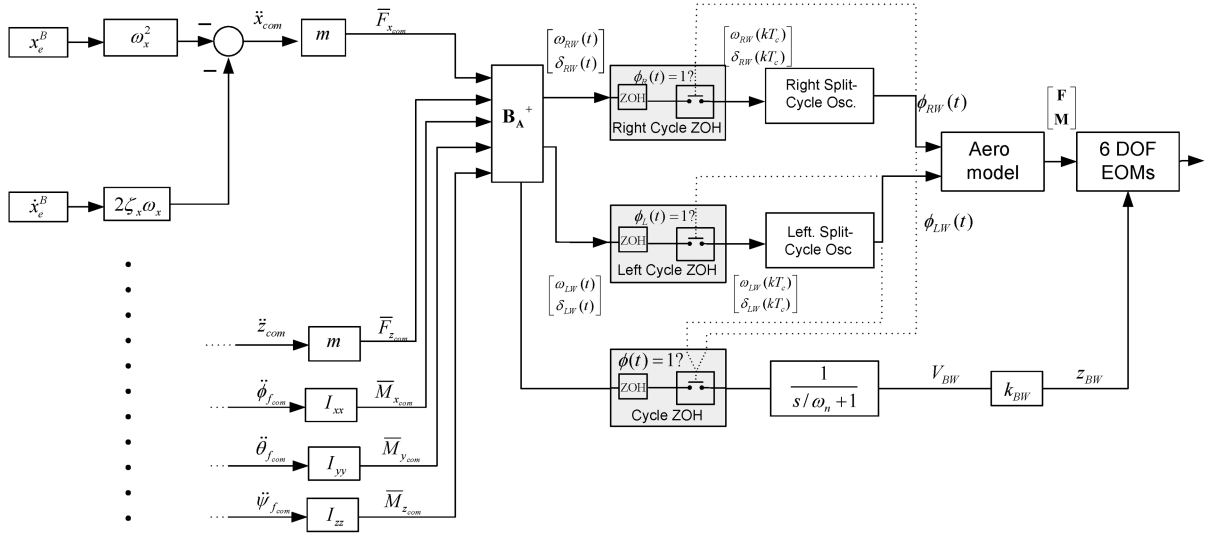


Fig. 6 Five-degree-of-freedom split-cycle controller.

actuator commands. Additionally, near the hover condition, the equations of motion reduce to a bank of decoupled double integrators, because there are no aerodynamic forces acting on the fuselage other than those produced by the beating wings, which are accounted for in the control effectiveness matrix. Thus, each axis is considered as a simple second-order one-dimensional system:

$$\ddot{x} = u \quad (73)$$

Defining χ_d as a desired reference command, it is well-known that assigning $u = -\omega_n^2(\chi - \chi_d) - 2\zeta\omega_n(\dot{\chi} - \dot{\chi}_d)$ forces the response of the system to that of a second-order damped harmonic oscillator with natural frequency ω_n and damping ratio ζ . This simple view is applied to each degree of freedom of the system. A feedback structure is assigned to the commanded cycle-averaged forces and moments as follows:

$$\begin{aligned} \bar{F}_{x_{com}}^B &= (-x_e^B\omega_{Fx}^2 - \dot{x}_e^B 2\zeta_{Fx}\omega_{Fx})m \\ \bar{F}_{z_{com}}^B &= (-z_e^B\omega_{Fz}^2 - \dot{z}_e^B 2\zeta_{Fz}\omega_{Fz})m \\ \bar{M}_{x_{com}}^B &= (-\phi_e\omega_{Mx}^2 - p_e 2\zeta_{Mx}\omega_{Mx})I_{xx} \\ \bar{M}_{y_{com}}^B &= (-\theta_e\omega_{My}^2 - q_e 2\zeta_{My}\omega_{My})I_{yy} \\ \bar{M}_{z_{com}}^B &= (-\psi_e\omega_{Mz}^2 - r_e 2\zeta_{Mz}\omega_{Mz})I_{zz} \end{aligned} \quad (74)$$

A block diagram of the control structure is shown in Fig. 6. An alternative view is to consider the structure as a sequential loop

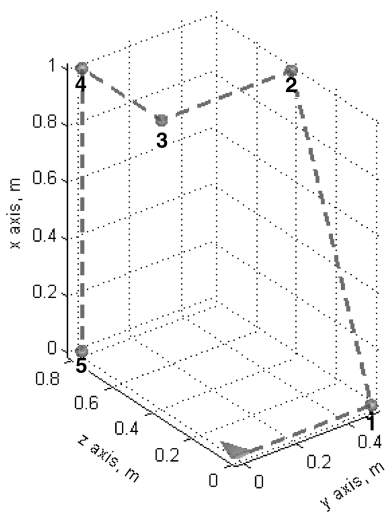


Fig. 7 Desired trajectory.

closure controller that uses proportional-derivative feedback, where the gains are tuned by choosing appropriate values for each ω_n and ζ , in Eq. (74).

Note that the y -axis translation is not directly controlled, in the sense that there is no $\bar{F}_{y_{com}}^B$. Instead, the y -axis translation is regulated by injecting y_e into the desired yaw assigned by an outer-loop controller, which is described in the subsequent section. Assuming a nominal \bar{F}_x^B cycle-averaged force equal to weight, mg , and zero side force, then elementary trigonometry shows that at zero pitch and roll, the force directed along the y inertial frame axis is $\sin(\psi)mg$, or ψmg with a small angle approximation. This simplified analysis is employed to construct a desired approximate side translation force, through an added desired yaw. The added desired yaw has the same feedback gain structure as the inner-loop feedback, and is given by

$$\hat{\psi}_d = (-y_e^B\omega_{yn}^2 - \dot{y}_e^B 2\zeta_y\omega_{yn})\frac{1}{g} \quad (75)$$

The y translation reference command $\hat{\psi}_d$ appears in the outer-loop controller presentation.

C. Control Allocation

A pseudo-inverse control allocation scheme [24] is used to determine the necessary control inputs to produce the desired cycle-averaged forces and moments. The control allocator computes the fundamental frequencies, split-cycle parameters, and voltage applied

Table 4 Properties of proposed flapping-wing MAV

Variable	Value	Units
m_o	60	mg
m_{bw}	20	mg
Height	11	mm
Width	4	mm
Depth	1	mm
I_A	1395	mm ⁴
k_{BW}	$0.165e - 5$	Volt/mm
Nominal CG location	[5.5 0 0]	mm
c_{max}	4	mm
d_b	3	mm
R	15	mm
Δr_R^B	[3.5 2 0]	mm
Δr_L^B	[3.5 -2 0]	mm
α_U	45	deg
α_D	45	deg
Hover frequency	113.61	Hz
$=\omega_o = \sqrt{\frac{mg}{.5\rho C_L(\alpha)I_A}}$		

Table 5 Inner-loop and *y*-body-axis regulation controller parameters

Tuning parameter	Value
ω_{Fx_n}	7
ζ_{Fx_n}	1
ω_{Fy_n}	7
ζ_{Fy_n}	1
ω_{Fz_n}	4
ζ_{Fz_n}	.85
ω_{Mx_n}	40
ζ_{Mx_n}	1
ω_{My_n}	98
ζ_{My_n}	2.7
ω_{Mz_n}	30
ζ_{Mz_n}	1.1

to the bob-weight actuator based on the cycle-averaged force and moment commands. The fundamental frequencies and split-cycle parameters govern the behavior of oscillators that generate time-varying wing position commands. Inputs to the oscillators are held constant over the course of a wingbeat in order to avoid changing the shape of the split-cycle waveform in midcycle. The element used to accomplish this function is called a cycle zero-order hold. The output of the oscillators are applied to the bimorph piezoelectric actuators. It is assumed that the actuator bandwidth is sufficient to track the wing position commands.

Given the control variable vector $\mathbf{u} = [\delta_{RW} \ \Delta\omega_{RW} \ \delta_{LW} \ \Delta\omega_{LW} \ V_{BW}]^T$ and hover condition $\mathbf{u}_o = [0, \ \omega_o, \ 0, \ \omega_o, \ 0]^T$, the control allocation at time t_k is expressed as follows:

$$\mathbf{u}(t_k) = \mathbf{B}_A^+ \bar{\mathbf{G}}_{\text{com}}(t_k) + \mathbf{u}_o \quad (76)$$

where

$$\bar{\mathbf{G}}_{\text{com}} = [\bar{F}_{x_{\text{com}}}^B \ 0 \ \bar{F}_{z_{\text{com}}}^B \ \bar{M}_{x_{\text{com}}}^B \ \bar{M}_{y_{\text{com}}}^B \ \bar{M}_{z_{\text{com}}}^B]^T \quad (77)$$

and \mathbf{B}_A^+ denotes the pseudo-inverse of \mathbf{B}_A . The structure of the control allocation matrix is simplified because the split-cycle control strategy yields a highly decoupled control effectiveness matrix. Note that the term $\bar{F}_{y_{\text{com}}}^B$ is identically set to zero, since direct side force cannot be generated using the split-cycle method and that side-force corrections are made by adjustments to yaw attitude.

VIII. Outer-Loop Controller

The outer-loop controller generates the desired position and orientation, with respect to the inertial coordinate frame, which is fed to the error generator. This includes the tasks of providing desired trajectories for waypoint tracking and regulating the *y*-axis translation by generating a desired yaw, since the inner-loop does not directly regulate *y* translation. The desired position and orientation vary as step changes are fed through second-order continuous-time smoothing filters.

$$\mathbf{R}_I^D = \begin{pmatrix} \cos(\psi_d) \cos(\theta_d) & \sin(\psi_d) \cos(\phi_d) + \cos(\psi_d) \sin(\theta_d) \sin(\phi_d) & \sin(\psi_d) \sin(\phi_d) - \cos(\psi_d) \sin(\theta_d) \cos(\phi_d) \\ -\sin(\psi_d) \cos(\theta_d) & \cos(\psi_d) \cos(\phi_d) - \sin(\psi_d) \sin(\theta_d) \sin(\phi_d) & \cos(\psi_d) \sin(\phi_d) + \sin(\psi_d) \sin(\theta_d) \cos(\phi_d) \\ \sin(\theta_d) & -\cos(\theta_d) \sin(\phi_d) & \cos(\theta_d) \cos(\phi_d) \end{pmatrix}$$

The waypoint reference generator computes a desired trajectory for the inner-loop controller based on a roll-and-translate approach, which is similar to a bank-to-turn strategy. The approach is to use the roll angle to first adjust the heading angle of the hovering vehicle, such that the positive *z* axis of the body frame is directed towards the waypoint. Then, the aircraft translates to the waypoint while the attitude is regulated. Hence, the desired position is the waypoint itself and the desired orientation has zero pitch and yaw attitude, but the roll is determined by the desired heading. The separation of these two

operations is relaxed by replacing the demand of perfect alignment of the *z* body axis with requiring that the *z* axis be within $\bar{\phi}$ of being directed towards the waypoint, creating a $2\bar{\phi}$ -wide heading window. Furthermore, once the projection of the vehicle's position on the (*y*, *z*) plane of the inertial frame is within distance \bar{x} of the waypoint, the desired orientation is not allowed to change, creating a position window of radius \bar{x} . The position window prevents the outer-loop controller from perpetually prescribing oscillating roll commands as the vehicle cycles about the desired waypoint.

Without loss of generality, it is assumed that the initial position before a waypoint change is zero and that the vehicle is hovering; i.e., the *x* axis of the body frame is vertical. Given waypoint $\mathbf{x}_{\text{wp}}^l = (x_{\text{wp}} \ y_{\text{wp}} \ z_{\text{wp}})^T$, the waypoint orientation is computed as

$$\Phi_I^{\text{wp}} = \begin{pmatrix} \phi_{\text{wp}} \\ \theta_{\text{wp}} \\ \psi_{\text{wp}} \end{pmatrix} = \begin{pmatrix} \arctan(-(y_{\text{wp}} - y), (z_{\text{wp}} - z)) \\ 0 \\ 0 \end{pmatrix} \quad (78)$$

where $\mathbf{x}' = [x \ y \ z]^T$ is the position of the vehicle and ϕ_{wp} is the desired heading derived from elementary trigonometry, expressed in terms of a four-quadrant inverse tangent. The $\hat{\Phi}_I^D$ vector denotes the additional attitude command generated by feedback. This vector consists only of $\hat{\psi}_d$ from Eq. (75), but additional commands, such as a desired pitch, can be generated to assist forward/backward translation.

The desired orientation is generated as follows:

$$\Phi_I^D = \begin{cases} \mathbf{G}_o(\bar{\Phi}_I^D) + \hat{\Phi}_I^D & \text{if } \sqrt{(y - y_{\text{wp}})^2 + (z - z_{\text{wp}})^2} \leq \bar{x} \\ \mathbf{G}_o(\Phi_I^D) + \hat{\Phi}_I^D & \text{otherwise} \end{cases} \quad (79)$$

where $\mathbf{G}_o(\cdot)$ represents a second-order filter bank with natural frequency and damping ratio $\omega_{\Phi_I^D}$, $\zeta_{\Phi_I^D}$, respectively, and $\bar{\Phi}_I^D$ is the value of Φ_I^D , held from the instant when the condition $\sqrt{(y - y_{\text{wp}})^2 + (z - z_{\text{wp}})^2} \leq \bar{x}$ was most recently satisfied. The filter \mathbf{G}_o is used to maintain differential continuity of the desired orientation after a discrete waypoint change. Note that the position condition in (79) is a condition on the difference between the position of the vehicle and the waypoint, projected on the (*y*, *z*) plane of the inertial frame; it is not a function of the desired position described below.

Because of the body frame orientation at hover, it is convenient to consider Φ_I^D as a 1-2-3 rotation. This is comparable to the common 3-2-1 rotation for a standard aircraft in level flight, where the nose is directed forward along the *x* axis and the *z* axis is directed downward, while the flapping-wing vehicle at hover is oriented such that its ventral side is directed forward along the *z* axis and the *x* axis is directed upward. The construction of $\hat{\Phi}_I^D$ and Φ_I^{wp} is thus made simple, with ϕ_d as the desired heading of the vehicle. The rotation matrix for $\Phi_I^D = [\phi_d, \ \theta_d, \ \psi_d]^T$ is

which is used in the error generation, Eq. (72), to compute the attitude error.

The desired position is computed as

$$\mathbf{x}_d^l = \begin{cases} G_p(\mathbf{x}_{\text{wp}}^l) & \text{if } |(\phi_d - \hat{\phi}_d) - \phi_{\text{wp}}| \leq \bar{\phi} \\ \bar{\mathbf{x}}_{\text{wp}}^l & \text{otherwise} \end{cases} \quad (80)$$

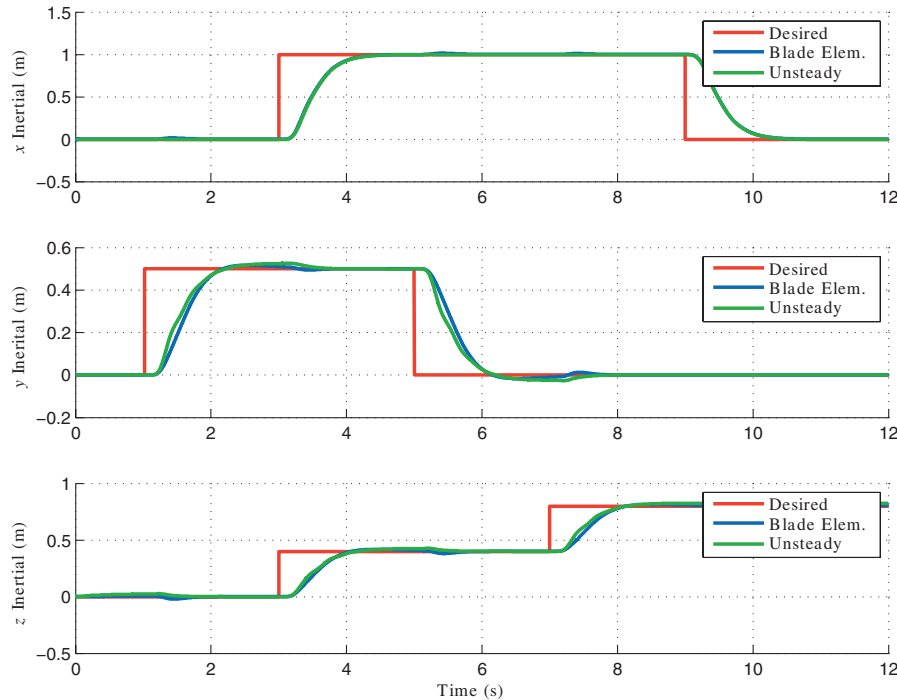
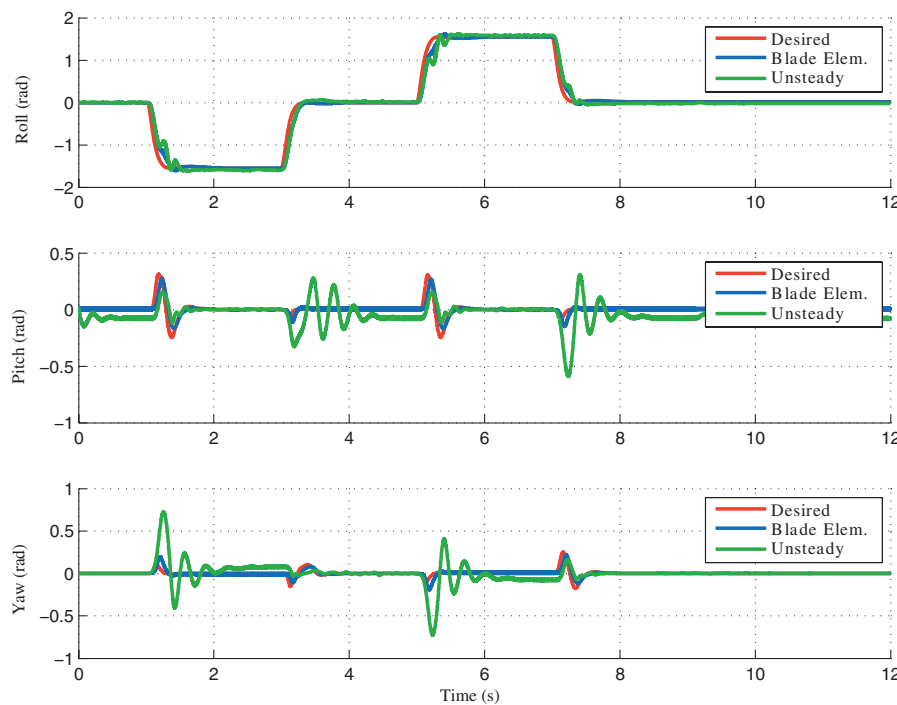
where $G_p(\cdot)$ represents a second-order filter with natural frequency and damping ratio $\omega_{x_{\text{wp}}^l}$, $\zeta_{x_{\text{wp}}^l}$, respectively, and $\bar{\mathbf{x}}_{\text{wp}}^l$ is the value of

Table 6 Outer-loop controller and filter parameters

Tuning parameter	Value
G_p natural frequency	4
G_p damping ratio	1
G_o natural frequency	20
G_o damping ratio	1
\bar{x}	$5 \cdot 10^{-2}$ m
$\bar{\phi}$	75°

$G_p(\mathbf{x}_{wp}^I)$, held from the instance when the condition $|(\phi_d - \hat{\phi}_d) - \phi_{wp}| \leq \bar{\phi}$ was most recently satisfied. The filter G_p is used to maintain differential continuity of the desired orientation after a discrete waypoint change.

The conditions in Eqs. (79) and (80), representing the heading and position windows, depends on the position of the vehicle, projected on the (y, z) plane of the inertial frame. In the case of Eq. (80), the dependency originates from the waypoint orientation Eq. (78), which depends on the position of the vehicle. The window is set such that the controller can be tuned to render a subset of the interior of the window attractive.

**Fig. 8** Inertial position time history resulting from waypoint tracking test using blade-element and unsteady simulations.**Fig. 9** Attitude time history resulting from waypoint tracking test using blade-element and unsteady simulations.

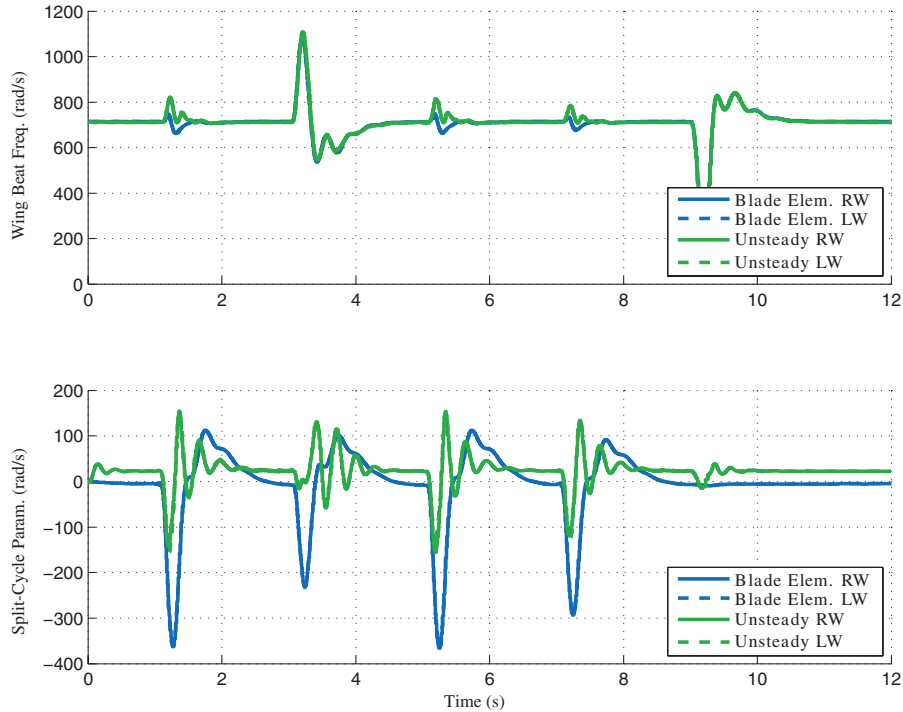


Fig. 10 Time history of fundamental and split-cycle frequencies resulting from waypoint tracking test using blade-element and unsteady simulations.

IX. Results

Figure 7 shows a three-dimensional trajectory that the vehicle is commanded to follow. The vehicle begins at the origin in inertial space; waypoints 1 through 5 are then fed to the outer-loop controller at 2-s intervals in ascending order. Vehicle properties are shown in Table 4. The inner- and outer-loop control parameters used to generate the subsequent simulation results are provided in Tables 5 and 6, respectively.

Figures 8 and 9 show the commanded and actual positions and attitudes of the vehicle center of gravity used to achieve waypoint following resulting from the instantaneous blade-element and

unsteady aerodynamic simulations. In both cases, tracking performance is acceptable and the vehicle is capable of performing the desired maneuvers; however, the performance in the unsteady aerodynamic simulation is noticeably degraded due to larger modeling errors. Figure 10 shows the resulting left and right wing fundamental and split-cycle frequencies. It can be observed that the left and right wing fundamental and split-cycle frequencies are significantly more dynamic in the unsteady aerodynamic simulation than those that were generated in the blade-element simulation. In both cases, differences between the left and right split-cycle frequencies result in the production of rolling and yawing moments

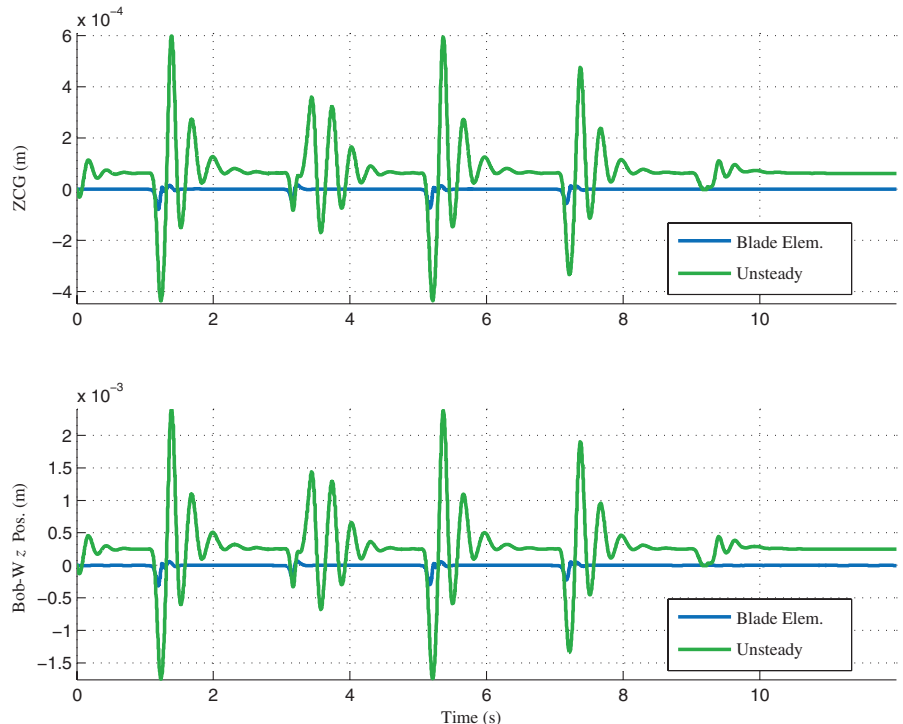


Fig. 11 Bob-weight position and cg shift in z body direction due to bob-weight movement; waypoint tracking test using blade-element and unsteady simulations.

that are used to align the vehicle's heading with the next waypoint and to regulate lateral translation. The position of the bob-weight and the location of the vehicle center-of-gravity in the z body-axis direction are shown in Fig. 11. In the blade-element simulation, it can be seen that the bob-weight shifts the center of gravity by about -0.08 mm in the worst case. This corresponds to a -0.32 mm shift in the z position of the bob-weight. In the unsteady simulation, it can be observed that bob-weight activity is much higher. The bob-weight shifts the center of gravity by up to 0.6 mm in the worst case, which corresponds to a 2.2 mm shift in the z position of the bob-weight. The magnitude of the required bob-weight in the unsteady aerodynamic simulation movement is considered excessive and might necessitate the use of an alternative actuator because of the limited range of motion of bimorph piezoelectric actuators. Mechanical amplification of the bimorph tip motion or an alternative pitch control strategy may have to be employed in practice.

X. Conclusions

Modeling and control of a flapping-wing MAV were considered in this manuscript. The results support the conclusion that it is possible to independently control vertical and horizontal forces as well as rolling and yawing moments using two physical actuators that allow the angular velocity profiles of the left and right wings to vary from upstroke to downstroke. The addition of an actuated bob-weight enabled control of the aircraft pitching moment. A method called split-cycle constant-period frequency modulation generated the required wingbeat actuator position commands and resulted in a high level of input decoupling, which enabled controllers with a simple structure to successfully provide controlled maneuverability in the vicinity of hover. The method has the desirable feature that cycle-averaged forces and moments can be analytically related to the wingbeat kinematics and vehicle design parameters, a feature that facilitates multidisciplinary design efforts where controllability must be considered from the outset. Additionally, simulation results reveal that a model-based control law, derived from a cycle-averaged blade-element aerodynamic model, can successfully control simulation models that include unsteady aerodynamic effects.

References

- [1] Deng, X., Schenato, L., Wu, W. C., and Sastry, S. S., "Flapping Flight for Biomimetic Robotic Insects, Part 1: System Modeling," *IEEE Transactions on Robotics and Automation*, Vol. 22, No. 4, 2006, pp. 776–788.
- [2] Deng, X., Schenato, L., Wu, W. C., and Sastry, S. S., "Flapping Flight for Biomimetic Robotic Insects, Part 2: Flight Control Design," *IEEE Transactions on Robotics and Automation*, Vol. 22, No. 4, 2006, pp. 789–803.
- [3] Khan, Z. A., and Agrawal, S. K., "Control of Longitudinal Flight Dynamics of a Flapping-Wing Micro Air Vehicle Using Time-Averaged Model and Differential Flatness Based Controller," *Proceedings of the American Control Conference*, IEEE, New York, July 2007, pp. 5284–5289.
- [4] Dileo, C., and Deng, X., "Design of and Experiments on a Dragonfly-Inspired Robot," *Advanced Robotics*, Vol. 23, Nos. 7–8, 2009, pp. 1003–1021.
doi:10.1163/156855309X443160
- [5] de Croon, G. C. H. H., de Clercq, K. M. E., Ruijsink, R., Remes, B., and de Wagter, C., "Design, Aerodynamics, and Vision-Based Control of the DelFly," *International Journal of Micro Air Vehicles*, Vol. 1, No. 2, June 2009, pp. 71–97.
- [6] Jones, K. D., Bradshaw, C. J., Papadopoulos, J., and Platzer, M. F., "Bio-Inspired Design of Flapping-Wing Micro Air Vehicles," *Aeronautical Journal*, Vol. 109, No. 1098, Aug. 2005, pp. 385–393.
- [7] Chung, S. J., Stoner, J. R., and Dorothy, M., "Neurobiologically Inspired Control of Engineered Flapping Flight," AIAA Paper 2009-1929, April 2009.
- [8] Sun, M., and Xiong, Y., "Dynamic Flight Stability of a Hovering Bumblebee," *Journal of Experimental Biology*, Vol. 208, No. 3, 2005, pp. 447–459.
doi:10.1242/jeb.01407
- [9] Ellington, C. P., "The Novel Aerodynamics of Insect Flight: Applications to Micro Air Vehicles," *Journal of Experimental Biology*, Vol. 202, No. 23, 1999, pp. 3439–3448.
- [10] Taylor, G. K., Bomphrey, R. J., and 't Hoen, J., "Insect Flight Dynamics and Control," AIAA Paper 2006-32, Jan. 2006.
- [11] Dietl, J. M., and Garcia, E., "Stability in Ornithopter Longitudinal Flight Dynamics," *Journal of Guidance, Control, and Dynamics*, Vol. 31, No. 4, 2008, pp. 1157–1163.
doi:10.2514/1.33561
- [12] Doman, D. B., Oppenheimer, M. W., and Bolender, M. A., "Altitude Control of a Single Degree of Freedom Flapping Wing Micro Air Vehicle," AIAA Paper 2009-6159, Aug. 2009.
- [13] Wood, R. J., "The First Takeoff of a Biologically Inspired At-Scale Robotic Insect," *IEEE Transactions on Robotics and Automation*, Vol. 24, No. 2, 2008, pp. 341–347.
- [14] Ellington, C. P., "The Aerodynamics of Hovering Insect Flight 3: Kinematics," *Philosophical Transactions of the Royal Society of London, Series B: Biological Sciences*, Vol. 305, No. 1122, 1984, pp. 41–78.
doi:10.1098/rstb.1984.0051
- [15] Wood, R. J., Steltz, E., and Fearing, R. S., "Optimal Energy Density Piezoelectric Bending Actuators," *Sensors and Actuators, A: Physical*, Vol. 119, No. 2, 2005, pp. 476–488.
doi:10.1016/j.sna.2004.10.024
- [16] Willmott, A. P., and Ellington, C. P., "The Mechanisms of Flight in the Hawkmoth *Manduca Sexta*, 1: Kinematics of Hovering and Forward Flight," *Journal of Experimental Biology*, Vol. 200, No. 21, 1997, pp. 2705–2722.
- [17] Ennos, A. R., "The Kinematics and Aerodynamics of the Free Flight of Some Diptera," *Journal of Experimental Biology*, Vol. 142, No. 1, 1989, pp. 49–85.
- [18] Doman, D. B., Oppenheimer, M. W., and Sigthorsson, D. O., "Dynamics and Control of a Minimally Actuated Biomimetic Vehicle, Part 1: Aerodynamic Model," AIAA Paper 2009-6160, Aug. 2009.
- [19] Oppenheimer, M. W., Doman, D. B., and Sigthorsson, D. O., "Dynamics and Control of a Minimally Actuated Biomimetic Vehicle, Part 2: Control," AIAA Paper 2009-6161, Aug. 2009.
- [20] Sane, S. P., and Dickinson, M. H., "The Control of Flight Force by a Flapping Wing: Lift and Drag Force Production," *Journal of Experimental Biology*, Vol. 204, No. 15, 2001, pp. 2607–2626.
- [21] Gradshteyn, I. S., and Ryzhik, I. M., *Table of Integrals, Series and Products*, 6th ed., Academic Press, New York, 2000, pp. 414–415.
- [22] Doman, D., and Ngo, A., "Dynamic Inversion-Based Adaptive/Reconfigurable Control of the X-33 on Ascent," *Journal of Guidance, Control, and Dynamics*, Vol. 25, No. 2, 2002, pp. 275–284.
doi:10.2514/2.4879
- [23] Etkin, B., *Dynamics of Atmospheric Flight*, Wiley, New York, 1972, p. 117.
- [24] Schierman, J., Ward, D., Hull, J., Gandhi, N., Oppenheimer, M., and Doman, D., "Integrated Adaptive Guidance and Control for Re-Entry Vehicles with Flight Test Results," *Journal of Guidance, Control, and Dynamics*, Vol. 27, No. 6, 2004, pp. 975–988.
doi:10.2514/1.10344